

# **Anisotropic microstructures of Au and Ag**

**A thesis**

**Submitted in partial fulfillment of the  
requirements of the degree of  
Master of Science [Engg.]**

**by**

**Gangaiah Mettela**



**Chemistry and Physics of Materials Unit  
JAWAHARLAL NEHRU CENTRE FOR ADVANCED  
SCIENTIFIC RESEARCH**

**(A Deemed University)**

**BANGALORE, INDIA**

**January 2012**

*Dedicated to my brother Anil Veerla*

## DECLARATION

I hereby declare that the thesis entitled “*Anisotropic microstructures of Au and Ag*” is an authentic record of research work carried out by me at the Chemistry and Physics of Materials Unit, Jawaharlal Nehru Centre for Advanced Scientific Research, Bangalore, India under the supervision of *Professor G. U. Kulkarni* and that it has not been submitted elsewhere for the award of any degree or diploma.

In keeping with the general practice in reporting scientific observations, due acknowledgment has been made whenever the work described is based on the findings of other investigators. Any omission that might have occurred due to oversight or error in judgment is regretted.

Gangaiah Mettela

## CERTIFICATE

Certified that the work described in this thesis titled “*Anisotropic microstructures of Au and Ag*” has been carried out by Mr. Gangaiah Mettela at the Chemistry and Physics of Materials Unit, Jawaharlal Nehru Centre for Advanced Scientific Research, Bangalore, India under my supervision and that it has not been submitted elsewhere for the award of any degree or diploma.

Professor G. U. Kulkarni  
(Research Supervisor)

# Acknowledgements

I express my deep sense of gratitude to **Professor G. U. Kulkarni**, for being my research supervisor and guiding me in a right direction to approach and solve scientific problems. I am very grateful to him for suggesting such an interesting project and rejuvenating me with new explorations. His vision of science and problem solving approach is very inspiring. His simple way of thinking and reasoning is astounding. Imagining myself in his shoes, I wonder how he deals with such multi disciplinary fields of physics and chemistry. He always remains as a reference to me in choosing a research problem in the upcoming field to remain as a forefront researcher.

**Professor C. N. R. Rao** is a great source of inspiration and encouragement to me. I learned more about him through my research supervisor, who himself is a great disciple of him. My mentor used to take his example, saying how different as an individual he is to be so great and used to motivate us in doing a better science. His scientific lectures are appealing and encouraging to young scientists. His words always ring in my ears, as he says *“Research makes a person younger with time”*.

I thank all the faculty members of CPMU and NCU for their cordiality, especially my teachers, Professor. N. Chandrabhas, Umesh Waghmare, Sundaresan, Eswaramoorthy, S. M. Shivaprasad, Drs. Subi, Govindraju, T. K. Maji and Prof. Guru Row (IISc) for their courses.

I thank Mrs. Indira Kulkarni, Teju and poorna for their warmth and hospitality.

I am grateful to my labmates, Dr. Abhay A Sagade, Dr. Rashmi, B. Radha, Narendra Kurra, Ritu Gupta, K.D.M. Rao, Umesha Mogera, S. Kiruthika, Ankush, Vandana, Tripura and Veeresh for their support and friendly nature.

Timely and ready assistance and also friendly attitude from technical staff, Mr. Srinath and Mr. Srinivas is acknowledged. I am very thankful to Mrs. Usha (TEM), Mrs. Selvi (FESEM) and Mrs. Suma (Confocal microscopy), Dr. Basavaraj (AFM), Mr. Anil (XRD), Mr. Mahesh (SEM), Mr. Kishore (XPS), Dr. Karthik (FIB), Mr. Vasu (UV) and Mr. A. Srinivasa Rao for their invaluable technical assistance. Ms. Vanitha and Mr. Sunil for their help in various lab activities.

I thank Drs. Leela Srinivas, Neenu Vargheese, Rakesh, Mr. Srinu Bhadram, Subramanyam, Gopal for Raman measurements.

I thank Prof. Sampath, Prof. A.K. Shukla, Dr. Sridhar, Dr. Ranjan Datta, Dr. Sundraiah, Partho da, Gayatri, Soumik, Dhanya, for their useful discussion

I thank my friends Vijay, Venkatesh, Kiran, Suresh, Tiru, Subbu, Dr.Suresh, Kishore, Venkateswarlu, Venkat Rao, mohit, Rama Krishna, Moses, Urmi, Ajmala, Gopal, Sunitha, Srinu, Morthy, Nitesh, Piyush, Pavan, Amirth, Venki, Nagarjun, Ramana Reddy, Rajdeep, Manasa, Manju, Loukya, Sowjanya, Sunitha, Sivani for their friendly nature.

I thank Dr. KKR Datta and Mrs. Datta for their hospitality and moral support.

I thank the staff of academic and administrative section in JNC for their assistance, especially Dr. Princy and Mrs. Sukanya for their advices and friendly nature. I also thank the library staff for their help. I am thankful to the computer lab staff and purchase office staff.

I thank CSIR for financial assistance and DST for providing facilities.

I thank my M.Sc friends Sirisha, Arjun, Chandrababu naidu, Annapoorna, Kishore, Kalyan, Lakshmi, Venky, Giri, Srikanth, Subbu, Venkateswarlu, Manjula, Ramky, Tyson and Jaggu for making my M.Sc days memorable.

All this effort becomes futile without acknowledging my beloved parents, sister and my friends Srikanth and Anusha, at the same it is impossible to express my gratitude to them without whose support and wish, I would have not come thus far. They are always ready to share my grief and joy and encourage me to do better than the best.

## Preface

The thesis pertains to synthesis of Au and Ag microstructures and their application as SERS substrates. It is arranged into three chapters.

**Chapter 1** introduces the concept of nanoscale materials and their important properties.

**Chapter 2** discusses the synthesis, optimization of size and shape of corrugated pentagonal bipyramidal Au microstructures ( $\mu$ -CPBs). It also deals with characterization, growth and the application of  $\mu$ -CPBs in SERS.

**Chapter 3** discusses the synthesis of various Ag nanostructures such as cubes, dendrites and polygons and their applications in SERS.

# Contents

Preface.....	vii
--------------	-----

## **Chapter 1. Introduction to Nanomaterials**

1.1 Introduction.....	1
1.2 Optical properties of metal nanostructures.....	3
1.3 Surface Enhanced Raman Spectroscopy.....	7
1.4 Electrical properties of metal nanostructures.....	9
1.5 Magnetic properties of metal nanostructures.....	11
1.6 Characterization techniques.....	12
References.....	14

## **Chapter 2. Synthesis of corrugated pentagonal bipyramidal Au microstructures ( $\mu$ -CPBs) and their applications in SERS**

Summary.....	17
2.1 Introduction.....	18
2.2 Scope of the Investigation.....	20
2.3 Experimental details .....	20
2.4 Results and discussion.....	21
2.4.a Synthesis and characterization of $\mu$ -CPBs.....	22
2.4.b Growth mechanism of $\mu$ -CPBs.....	32
2.4.c SERS measurements.....	36
2.5 Conclusions.....	39
References.....	40

## **Chapter 3. Synthesis of Ag microstructures and their applications in SERS**

Summary.....	45
3.1 Introduction.....	46
3.2 Scope of the investigation.....	46
3.3 Experimental details.....	46



3.4 Results and discussion.....	47
3.4.a Synthesis of Ag Cubes.....	47
3.4.b Synthesis of Ag Dendrites.....	50
3.4.c Synthesis of Ag polygons.....	53
3.4.d SERS measurements.....	56
3.5.e Metal Enhanced Fluorescence.....	59
3.5 Conclusions.....	60
References.....	61

## Abbreviations

ToABr	-	Tetraoctylammonium bromide
FESEM	-	Field emission scanning electron microscopy
AFM	-	Atomic force microscopy
XRD	-	X-ray diffraction
MEF	-	Metal-enhanced fluorescence
EBL	-	Electron beam lithography
FESEM	-	Field emission scanning electron microscopy
FTIR	-	Fourier transform infrared spectroscopy
SAED	-	Selected area electron diffraction
TGA	-	Thermal gravimetric analysis
CTAB	-	Cetyltrimethylammonium bromide
HOMO	-	Highest occupied molecular orbital
LUMO	-	Lowest occupied molecular orbital
TEM	-	Transmission electron microscopy
SWNT	-	Single walled carbon nanotube
SPR	-	Surface plasmon resonance
CPS	-	Counts per second

## Introduction to Nanomaterials

### 1.1 Introduction

The prefix nano in ‘nanoscience’ means a billionth ( $1 \times 10^{-9}$ ). It deals with various aspects of matter, having dimensions of the order of a billionth of a meter (1 nm). At the nanoscale, the fundamental properties of materials depend on their size, shape, and composition. When objects are below 100 nms in size, they tend to exhibit unusual chemical and physical properties [1].

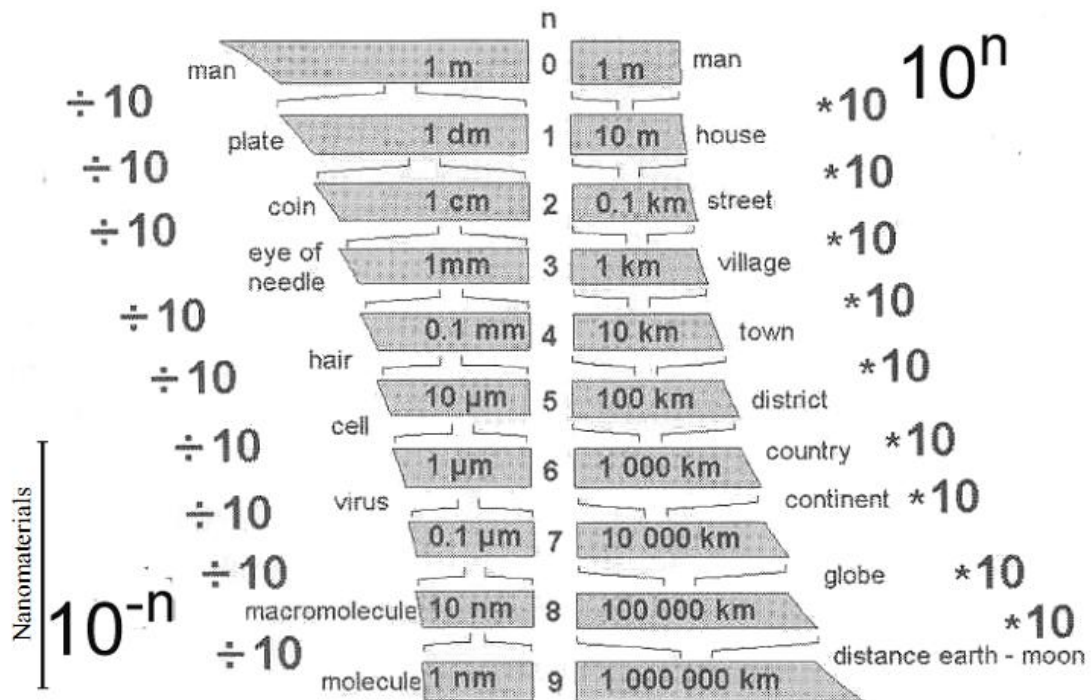


**Figure 1.1** Comparisons of objects are having different sizes from micrometer to nanometer [From ref 1].

For example, ZnO, an important semiconducting and piezoelectric material can be obtained in various shapes such as tubes, wires, rings and even other exotic forms such as springs, combs, belts and cages in nm range. Besides spherical nanoparticles of metals and semiconductors and carbon nanotubes [2, 3], other interesting shapes include nanotriangles, nanocubes, mesoflowers, nanoprisms, nanodisks and nanorings, junction nanotubes, nanowalls, nanoflowers etc. Such shapes may be derived from metals, semiconductors, oxides, nitrides, sulfides etc. Figure 1.2 shows electron micrographs of some interesting shapes of nanoobjects [4-10].

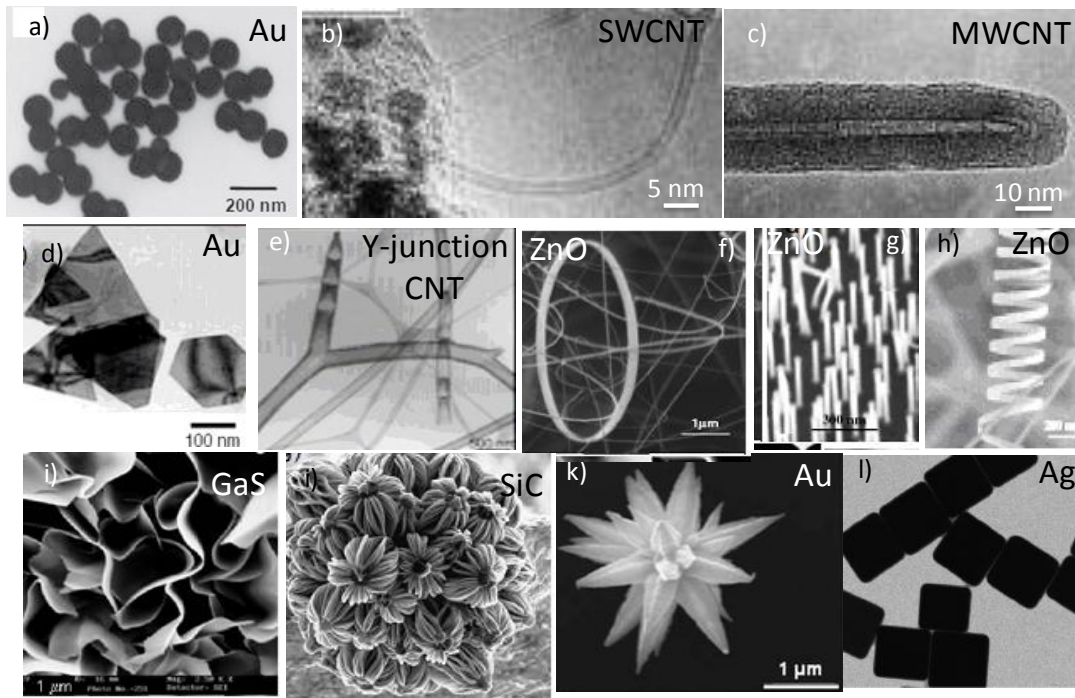


**Figure 1.2** Electron micrographs of nanomaterials in different shapes. a) Au nanosphericals b) SWCNT, c) MWCNT, d) Au nanotriangles. e) Y-junction CNTs. f), g) and h) ZnO nanoring, nanowires and nanospring. i) GaS nanowalls, j) SiC nanoflowers, k) Au mesoflower, l) Ag nanocubes [From ref 2-10].

The properties of a solid undergo dramatic changes when its physical dimensions of a solid become comparable to the mean free path of the electrons. This is known as quantum confinement. A schematic diagram of the density of states where the electrons are confined to one, two and three dimensions, named as 2D, 1D and 0D materials respectively, is given in Figure 1.3. Thus, materials that come under this regime are ultra-thin films (2D), nanotubes and nanorods (1D), nanoparticles or quantum dots (0D) of metals, semiconductors etc [11].

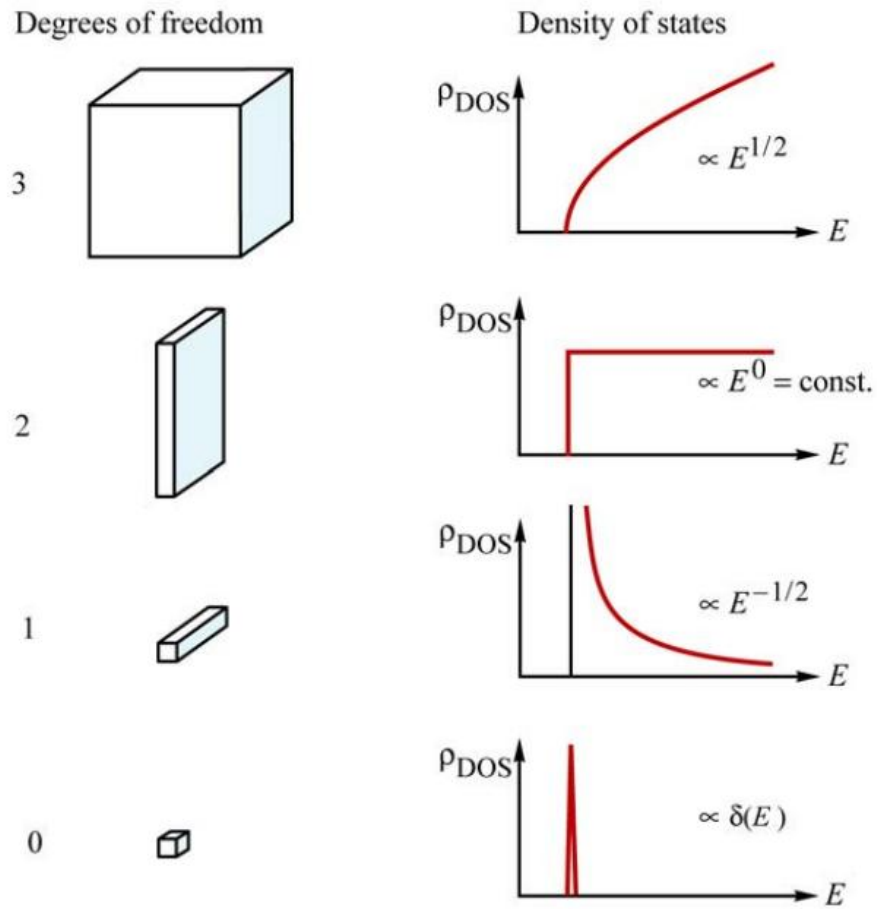


**Figure 1.3** Density of states for reduced dimensions [From ref 11].

The density of states in a 3, 2, and 1 dimensional systems has a functional dependence on energy according to  $E^{1/2}$ ,  $E$  and  $E^{-1/2}$  respectively [11], where  $E$  is the energy of the particle.

Below is a brief description related to metal nanostructures, which serve as case examples for nanomaterials in general.

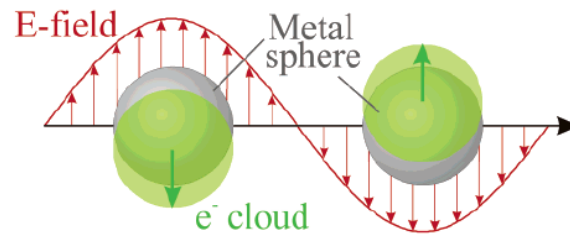
## 1.2 Optical properties of metal nanostructures

Metal nanostructures such as nanoparticles are quite interesting, because they exhibit localized surface plasmon resonance (LSPR) resulting in strong optical extinction at visible wavelengths. In LSPs, the electric field associated with the light ( $E_0$ ) applies a force on the gas of negatively charged electrons in the conduction band of the metal and drives them to oscillate collectively. At a certain excitation frequency ( $\omega$ ), this oscillation will be in resonance with the

# Chapter 1

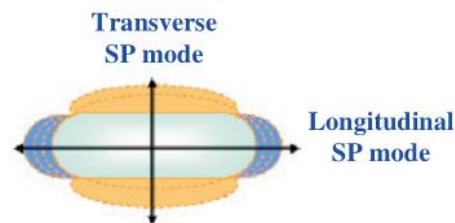
---

incident light, resulting in a strong oscillation of the surface electrons, commonly known as a localized surface Plasmon resonance (LSPR) mode [12, 13].













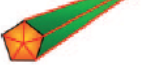


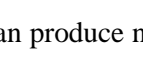
**Figure 1.4** Schematic of plasmon oscillation for a sphere, showing the displacement of the conduction electron charge cloud relative to the nuclei [From ref 13].

The chemical and physical properties of the metal nanoparticles are governed by physical parameters such as size, shape, composition and structure [14]. Among metals the coinage metals, Au, Ag and Cu have received attention as their absorption bands due to LSPR fall in visible region of electromagnetic spectrum. Based on the geometry, metal nanostructures could be classified into two types spherical and anisotropic structures. Table 1 illustrates the various reported morphologies for the nanoparticles of coinage metals and other metals [15]. The shape of a metal nanocrystal also plays a crucial role in deciding the optical properties which eventually effect their applications in various fields [16]. Spherical metal nanoparticles exhibit a single surface plasmon band attributed to the collective dipolar oscillation of the electron cloud. Au spherical np exhibit absorption related LSPR peak at ~540 nm while Ag spherical np ~420 nm. In the case of anisotropic structures, dipolar resonance split into two surface plasmon bands wherein the induced dipole oscillates along the transverse and longitudinal axes. Thus, the extinction spectrum of anisotropic metal nanoparticles consists two surface plasmon modes. They are longitudinal and transverse absorption peaks generated due to the electron oscillation parallel and perpendicular to the length of the particle as shown in Figure 1.5 [17].



**Figure 1.5** Schematic illustrating the electron oscillation parallel and perpendicular to the length of the rod [From ref 17].

Table 1: A summary of different shapes that have been achieved for various metal nanocrystals [From ref 15].

Structures	Shapes	Schematic drawings	Metals
single-crystal	perfect/truncated cube <sup>[b]</sup>		Pd, Ag, Au, Pt, Cu, Rh, Bi, Fe
	perfect/truncated octahedron <sup>[d]</sup>		Pd, Ag, Au, Pt
	perfect/truncated tetrahedron <sup>[a]</sup>		Ag, Au, Pt, Rh
	rectangular bar		Pd, Ag, Pt
	octagonal rod		Pd, Au, Fe, Co, Ni
	rectangular or octagonal wire		Pb, In, Sn, Sb, Fe, Co
singly twinned	right bipyramid		Pd, Ag
	beam		Ag
multiply twinned	decahedron <sup>[a]</sup>		Pd, Ag, Au
	icosahedron <sup>[b]</sup>		Pd, Au
	five-fold twinned pentagonal rod		Pd, Ag, Au, Cu
	five-fold twinned pentagonal wire		Ag, Au, Cu
	triangular/hexagonal plate		Pd, Ag, Au, Cu, Pb, Bi, Co, Ni
	disc		Sn, Co

A small change in the particle geometry can produce noticeable changes in the plasmon peak [17]. The longitudinal surface plasmon band shifts to longer wavelengths with increase in aspect ratio, while the position of transverse surface plasmon band remains more or less unaffected. The ratio of the intensities of the longitudinal and transverse modes can be tuned based on the aspect ratio. The absorption spectrum of anisotropic particles can be tuned based on the aspect ratio of the nanoparticles. As the aspect ratio increases, there is red shift in the longitudinal peak position as shown in Figure 1.6 [18].

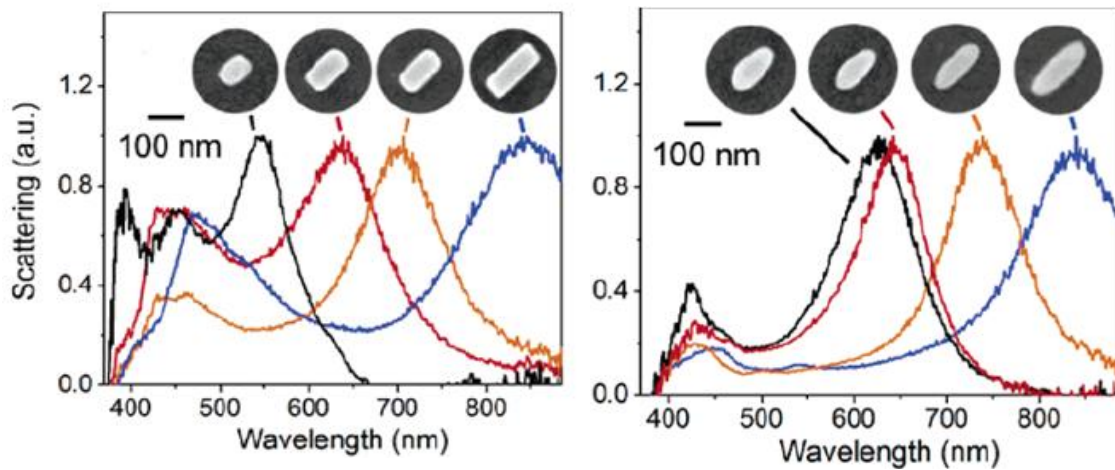


**Figure 1.6** SEM images of individual nanobars and rice with their corresponding normalized scattering spectra. The peaks of both nanobars and nanorice red shift with increasing length [From ref 18].

Among anisotropic metal nanoparticles, nanostructures having sharp features like tips, corners, edges etc., are more interesting. The sharpness of corners or edges of a nanostructure can have a great effect on the plasmonics properties of metal nanostructures. The sharp features alter the extinction spectrum drastically as shown in Figure 1.7. In general, structures with sharp corners have red shifted peaks when compared to rounded structures of similar sizes. Because the sharp features tend to increase charge separation and reduce the restoring force for the dipole oscillation, a reduction in resonance frequency or red-shift in wavelength is expected. Concentration of light in nanosized volumes increases electric field intensity at the sharp features [19]. This phenomenon has been known as *lightning rod effect* [20]. The electric field enhancement of anisotropic metal nanostructures is of immense interest in Raman spectroscopy.

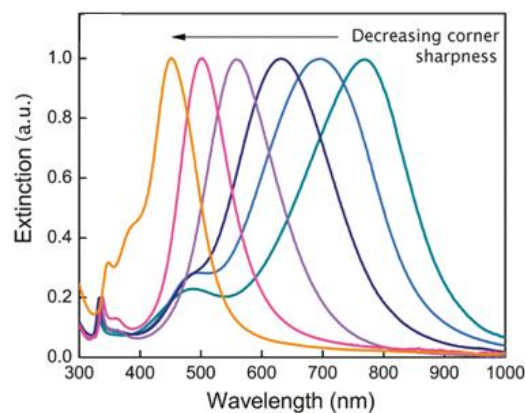


**Figure 1.7** The decreasing corner sharpness causes blue-shift in the extinction spectra of the silver nanoparticles [From ref 19].



### 1.3 Surface Enhanced Raman Spectroscopy

Molecules adsorbed on metal surfaces of nanostructures exhibiting nm scale roughness, the Raman signal intensity of the molecule is enhanced by many orders of magnitude. This phenomenon is called as Surface enhanced Raman scattering (SERS) [21, 22]. Earlier to the discovery of SERS, laser Raman scattering was not an ideal candidate to study vibration spectroscopy of molecules at low concentrations because the Raman cross section was too small when compared to other optical processes of a molecule. In a situation where a fluorescent molecule is under Raman scattering study, there is always a possibility that the Raman signal being masked due to the fluorescence back-ground. This is because the non-resonant Raman cross section of a molecule is around  $10^{-26}$  cm<sup>2</sup> per molecule, where as the fluorescence cross section of molecule is around  $10^{-17}$  cm<sup>2</sup> per molecule [23]. SERS has the ability to avoid this problem because the Raman cross section is no more the same as that for the conventional Raman scattering, but would be drastically changed to values comparable to Fluorescence. Since its discovery, this enhanced Raman cross section in SERS has been considered as a tool for ultra trace analysis of molecules. These two important enhancement mechanisms underlying the SERS phenomenon are called as Electromagnetic and Chemical enhancement mechanisms [24-26].

#### 1.3.1 Electromagnetic enhancement mechanism

At the near field of a metallic surface, the electric field is strong due to the surface plasmon resonance. Any molecule placed near a metallic surface is under the influence of this strong electric field  $E_M$  which is the super position of the incoming field and the a dipole field induced in the metal sphere. The field enhancement factor  $A(\nu)$  is the ratio of the field at the position of the molecule and the incoming field. The expression for this is as follows:

$$A(\nu) = \frac{E_M(\nu)}{E(\nu)} = \frac{\varepsilon - \varepsilon_0}{\varepsilon + 2\varepsilon_0} \left( \frac{r}{r+d} \right)^3.$$

The value of  $A(\nu)$  is large when the real part of  $\varepsilon_0$  is equal to  $-2\varepsilon_0$ . Additionally, for a strong electromagnetic enhancement, the imaginary part of the dielectric constant should be small. Metals like Ag, Au and Cu satisfy the above conditions at visible wavelengths, and hence exhibit SERS properties. As in the case of laser field, the Stokes or anti-Stokes field is enhanced if it is in resonance with the surface plasmons of the metal spheres. Taking into effect the enhancement due to laser field and the Stokes field, the electromagnetic enhancement factor for the Stokes scattering is given by

$$G_{em}(\nu_s) = |A(\nu_L)|^2 |A(\nu_S)|^2 = \left| \frac{\varepsilon(\nu_L) - \varepsilon_0}{\varepsilon(\nu_L) + 2\varepsilon_0} \right|^2 \left| \frac{\varepsilon(\nu_S) - \varepsilon_0}{\varepsilon(\nu_S) + 2\varepsilon_0} \right|^2 \left( \frac{r}{r+d} \right)^{12}$$

Following are the important implications of the above equation.

The enhancement scales as fourth power of the local field at the vicinity of the metallic nanostructure and is particularly strong when the scattered and the plasmon field are in resonance. The electromagnetic enhancement is a distance dependent mechanism. The enhancement decays as  $(r / (r + d))$ . Interestingly, it is not necessary for the molecule to be in contact with the metal surface to exhibit enhancement. The contribution of electromagnetic mechanism towards Raman signal enhancement is greater than any other mechanisms. It accounts for an enhancement factor of at least  $10^4$  to  $10^6$  in normal conditions [27].

### 1.3.2 Chemical enhancement mechanism

This mechanism is mainly attributed to electronic coupling between molecule and metal, and leads to formation of an adsorbate-surface complex, resulting in an increased Raman cross section of the adsorbed molecule in the complex compared with the cross section of a 'free' molecule in a 'normal' Raman experiment.

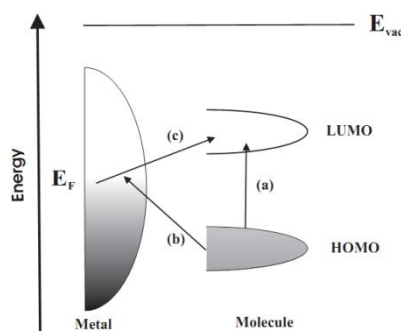


**Figure 1.8** Schematic for the chemical enhancement mechanism in SERS [From ref 22].

It leads to form a new (charge transfer) electronic transition in the metal-molecule system. This mechanism has mainly three steps.

- 1) The photon is absorbed by the metal nanostructures which results in a hot electron state.
- 2) The hot electron gets transferred into the LUMO of the molecule.

- 3) The hot electron is transferred from LUMO back to the metal nanostructures.
- 4) Return of the electron to its initial state by emitting Stokes photons.

The chemical enhancement mechanism contributes to an enhancement factor of 10 to 100 in magnitude [27].

#### 1.4 Electrical properties of metal nanostructures

As the properties become size dependent, a metal np may undergo metal-insulator transition (Figure 1.9). For example, Au and Ag are conducting in bulk whereas they are insulators in the nano dimensions.

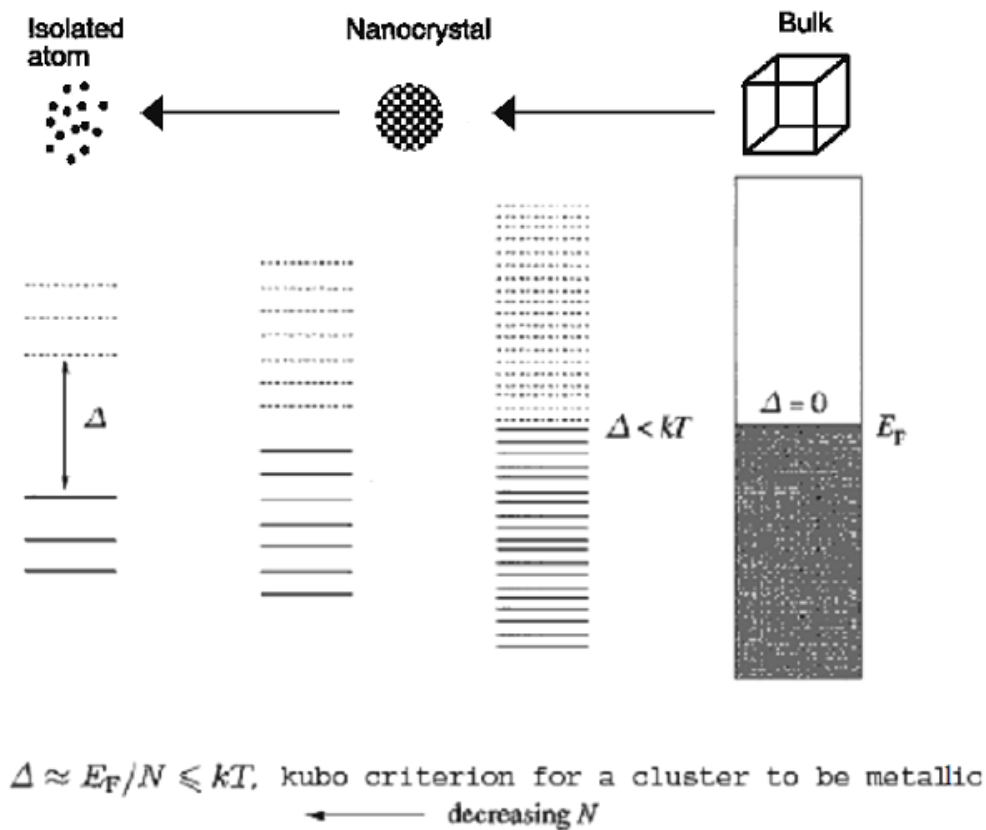


**Figure 1.9** Size induced effects in metallic nanocrystals [From ref 28].

However as the kubo gap very smaller compared to working temperatures, one requires to cool the nanoparticles to very low temperatures to observe insulating state of one metal. Nanoparticles possess columbic energy states that manifest themselves when actual charging and discharging events take place. Experiments have revealed that small nanocrystals possess charging

## Chapter 1

---

energies (U) of the order of hundreds of meV [29]. Therefore, in ensembles of nanocrystals, charge transport would be dominated by a hopping mechanism. Pellets made of small Au and Pd nanocrystals exhibit nonmetallic behavior with specific conductivities in the range of  $10^6 \Omega^{-1}\text{cm}^{-1}$ . The conductivity, however, increases dramatically with an increase in the diameter of the nanocrystals. An insulator metal transition has indeed been reported from pellets made of  $\sim 12.5$  nm Au and Ag nanocrystals. Conductivity of monolayered two-dimensional arrays of metal nanocrystals has been studied which can be enhanced by replacing alkanethiol with aromatic thiol in situ. Interaction energy of nanocrystals can be varied in such organizations, by changing the interparticle spacing either by the spacer length or by applying pressure in a Langmuir-Blodgett trough. The capacitance (C) of a nanoparticle is size dependent and is related to U by

$$C = \frac{U}{2e}$$

The classical expression for the capacitance of a metal sphere (of radius R) embedded in a dielectric with a dielectric constant,  $\epsilon_m$  is

$$C = 4\pi\epsilon\epsilon_m R.$$

Both these equations yield capacitances of the order of  $10^{-18}$  F (or 1 aF) for nanoparticles. In this regime of finite charging energies and low capacitances, the charging of a capacitor is no longer continuous, but is discrete. For a current to flow through a nanocrystal, an external voltage  $V_{\text{ext}}$  greater than  $e/2C$  is required. This phenomenon of current exclusion across zero bias is called Coulomb blockade. When the Coulomb blockade barrier is broken applying sufficient voltage, electrons tunnel into the nanocrystal and tunnel out almost immediately. The electrons may reside long enough to provide a voltage feedback preventing an additional electron from tunneling in simultaneously. A continuous one electron current, I given by  $I = e/2RC$  flows through the circuit. To place an additional electron on the nanocrystal, a full  $e/C$  increase in voltage is required. Thus, steps called a Coulomb staircase become visible in the IV spectra of nanocrystals. A schematic illustration of a Coulomb staircase observed in the I-V spectra is given in Figure 1.10 [30]. While Coulomb blockade is ordinarily observed, the observation of a Coulomb staircase requires a tuning of the circuit characteristics. It has been proposed that, by using nanocrystals, single electron devices such as supersensitive electrometers and memory devices could be fabricated [31].

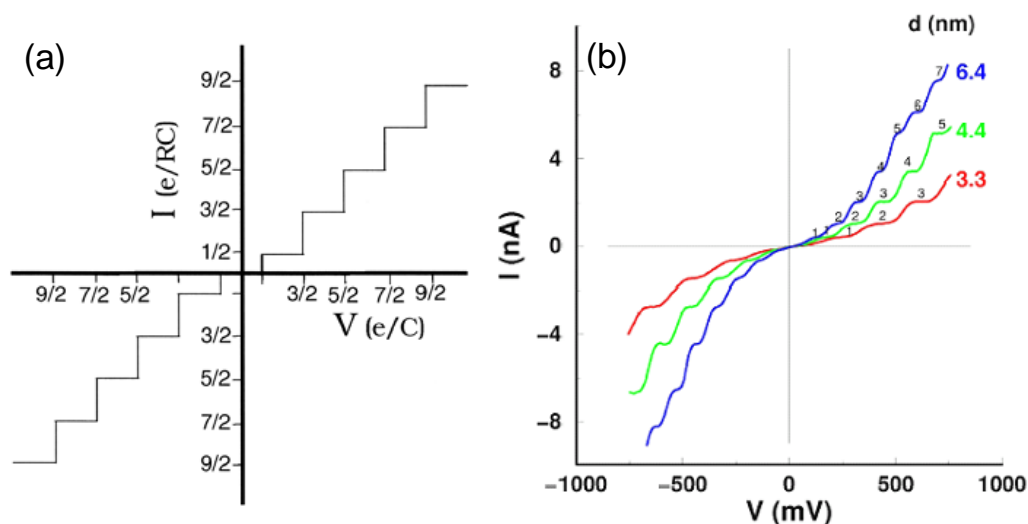


**Figure 1.10** (a) Schematic illustration of the Coulomb staircase behavior, (b) I-V spectra of Pd nanocrystals of different sizes exhibiting Coulomb staircase phenomena ( $U \sim 100$  meV) [From ref 30].

### 1.5 Magnetic properties of metal nanostructures

Magnetic particles of nanometer sizes are mostly single-domain, because the formation of domain walls becomes energetically unfavorable [32]. As particle size further decreases below the single-domain value, the magnetic moment of the particles are gradually affected by thermal fluctuation and they behave paramagnetic with giant moments. This ‘superparamagnetism’ has zero coercivity and readily occurs above a blocking temperature above which the thermal energy is sufficient for the moment to relax. The evolution of intrinsic coercivity,  $H_{CI}$ , as a function of particle size is illustrated in Figure 1.11. Above a critical particle size,  $D_S$ , the particles are multi-domain. The coercivity increases as the particle size decreases. Below,  $D_S$ , the particles are single-domain. When the average particle size decreases further below  $D_P$  the particles become superparamagnetic with unstable magnetic moments and vanishing coercivity. Stoner–Wohlfarth theory was developed to describe the behavior of an assembly of single-domain particles [33]. A more recent theory by Holz and Scherer addresses the coupling between magnetic particles in nanostructured materials [34]. The issue of exchange coupling between magnetic nanoparticles has drawn much attention in recent years, because it is expected to have significant impact on both the understanding and application of nanostructured magnetic materials.

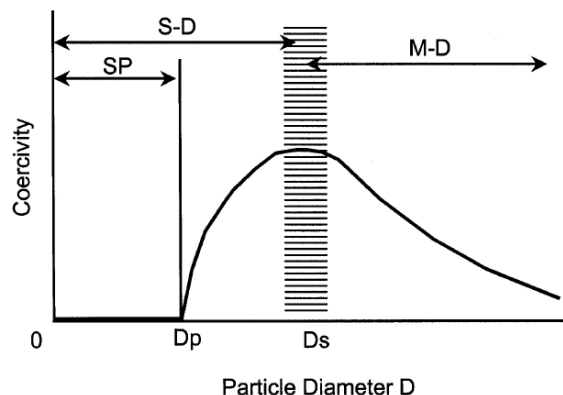


**Figure 1.11** Schematic illustration of the changes in the coercivity of a magnetic particle with change in the diameter. SP denotes the super paramagnetic regime, S-D the single domain regime and M-D the multi-domain regime [From ref 35].

Ferromagnetic particles become unstable when the particle size reduces below a certain size, since the surface energy provides a sufficient energy for domains to spontaneously switch polarization directions. As a result, ferromagnetics become paramagnetics. However, nanometer sized ferromagnetic turned to paramagnetic behaves differently from the conventional paramagnetic and is referred to as superparamagnetics.

Likewise almost every material property under goes change on size dependent at the nanoscale.

### 1.6 Characterization techniques

Several spectroscopic and microscopic techniques have been used to characterize the prepared samples reported in this thesis. In the following paragraphs, the details of instruments used and the sample preparation methods are described.

#### *X-ray diffraction*

Powder X-ray diffraction measurements were performed using a Siemens Seifert 3000TT diffractometer employing Cu K $\alpha$  ( $\lambda = 1.5406 \text{ \AA}$ ) radiation. Samples were prepared by depositing the nanomaterials in the form of films on glass slides and typical scan rate was  $1 \text{ deg.min}^{-1}$

#### *Thermogravimetric analysis*

Thermogravimetric analysis (TGA) was carried out (Mettler Toledo, TG-850) usually in the temperature range of  $30 \text{ }^\circ\text{C} - 300 \text{ }^\circ\text{C}$  at a heating rate of  $2 \text{ }^\circ\text{C.min}^{-1}$  in air. Typically using 10 mg of the sample in solid form mounted on a porcelain boat.

### *X-ray photo electron spectroscopy*

X-ray photoelectron Spectroscopy (XPS) measurements have been carried out using Omicron SPHERA spectrometer with non-monochromatic AlK $\alpha$  X-rays (E=1486.6 eV).

### *Atomic force microscopy*

Atomic force microscopy (AFM) experiments were carried out using Bruker diInnova Scanning Probe Microscope with Nanodrive controller. Imaging has been done in tapping Mode. TESP etched silicon cantilever probes of 125  $\mu\text{m}$  nominal length were used, at a drive frequency of approximately 240–280 kHz. Both height and amplitude information were recorded at a scan rate of 2–3 Hz, and stored in a 512-512 pixel format. Images were processed using the Nanoscope version 7.30 software. For optimum clarity in visual presentation of the images, flattening of first order was employed unless stated otherwise.

### *Transmission electron microscopy*

Transmission electron microscopy (TEM) measurements were carried out with a JEOL-3010 instrument operating at 300 kV ( $\lambda=0.0196\text{\AA}$ ) and electron diffraction (ED) patterns were collected at a camera length 20 cm (calibrated with respect to the standard polycrystalline Au thin film). Samples for TEM were prepared by depositing a drop of the nanomaterial (scraped from the substrate) on a holey carbon copper grid, allowing it to dry in a desiccator overnight.

### *Raman Measurements*

Raman measurements were performed using LabRAM HR apparatus (Horiba, USA) with an excitation wavelength of 632.8 nm and 5 mW.cm $^{-2}$ . Signal accumulation was performed for 10 s with a spot size of 1  $\mu\text{m}$ .

### *Scanning electron microscopy*

Scanning electron microscopy (SEM) was performed using a Nova NanoSEM 600 equipment (FEI Co., The Netherlands). Energy dispersive spectroscopic (EDS) mapping was performed using EDAX Genesis V4.52 (USA) attached to the SEM column. The EDS mapping was performed at 10 kV (energy window, 10 eV) with a beam current of 1.1 nA, the dwell time per pixel being 25  $\mu\text{s}$ . STEM (scanning transmission electron microscopy) and low vacuum imaging were performed on the same instrument using a STEM and helix detectors respectively.

# Chapter 1

---

## References

- [1] M. Köhler & W. Fritzsche N, Wiley VCH, Weinheim (2004).
- [2] Agrawal VV, Kulkarni GU, & Rao CNR (2008) Surfactant-promoted formation of fractal and dendritic nanostructures of gold and silver at the organic–aqueous interface. *Journal of Colloid and Interface Science* 318(2):501-506.
- [3] Rao CNR, Satishkumar BC, Govindaraj A, & Nath M (2001) Nanotubes. *ChemPhysChem* 2(2):78-105.
- [4] Ho GW, Wong ASW, Kang D-J, & Welland ME (2004) Three-dimensional crystalline SiC nanowire flowers. *Nanotechnology* 15(8):996.
- [5] Sajanalal PR & Pradeep T (2010) Magnetic Mesoflowers: Synthesis, Assembly, and Magnetic Properties†. *The Journal of Physical Chemistry C* 114(38):16051-16059.
- [6] Zhang Q, et al. (2010) Seed-Mediated Synthesis of Ag Nanocubes with Controllable Edge Lengths in the Range of 30–200 nm and Comparison of Their Optical Properties. *Journal of the American Chemical Society* 132(32):11372-11378.
- [7] Wang ZL (2004) Zinc oxide nanostructures: growth, properties and applications. *Journal of Physics: Condensed Matter* 16(25):R829.
- [8] Shankar SS, et al. (2004) Biological synthesis of triangular gold nanoprisms. *Nat Mater* 3(7):482-488.
- [9] Rao CNR & Govindaraj A (2002) Carbon Nanotubes from Organometallic Precursors. *Accounts of Chemical Research* 35(12):998-1007.
- [10] Gautam UK, Vivekchand SRC, Govindaraj A, & Rao CNR (2005) GaS and GaSe nanowalls and their transformation to Ga<sub>2</sub>O<sub>3</sub> and GaN nanowalls. *Chemical Communications* (31):3995-3997.
- [11] <http://www.ecse.rpi.edu/~schubert/Course-ECSE-6968%20Quantum%20mechanics/Ch12%20Density%20of%20states.pdf>
- [12] Rycenga M, et al. (2011) Controlling the Synthesis and Assembly of Silver Nanostructures for Plasmonic Applications. *Chemical Reviews* 111(6):3669-3712.
- [13] Kelly KL, Coronado E, Zhao LL, & Schatz GC (2002) The Optical Properties of Metal Nanoparticles: The Influence of Size, Shape, and Dielectric Environment. *The Journal of Physical Chemistry B* 107(3):668-677.
- [14] Lou XW, Archer LA, & Yang Z (2008) Hollow Micro-/Nanostructures: Synthesis and Applications. *Advanced Materials* 20(21):3987-4019.



- [15] Xia Y, Xiong Y, Lim B, & Skrabalak SE (2009) Cover Picture: Shape-Controlled Synthesis of Metal Nanocrystals: Simple Chemistry Meets Complex Physics? (*Angew. Chem. Int. Ed.* 1/2009). *Angewandte Chemie International Edition* 48(1):1-1.
- [16] Jain PK, Lee KS, El-Sayed IH, & El-Sayed MA (2006) Calculated Absorption and Scattering Properties of Gold Nanoparticles of Different Size, Shape, and Composition: Applications in Biological Imaging and Biomedicine. *The Journal of Physical Chemistry B* 110(14):7238-7248.
- [17] [www.ias.ac.in/pubs/splpubs/pjubileebook/53.pdf](http://www.ias.ac.in/pubs/splpubs/pjubileebook/53.pdf)
- [18] Wiley BJ, et al. (2007) Synthesis and Optical Properties of Silver Nanobars and Nanorice. *Nano Letters* 7(4):1032-1036.
- [19] Zeng J, Roberts S, & Xia Y (2010) Nanocrystal-Based Time–Temperature Indicators. *Chemistry – A European Journal* 16(42):12559-12563.
- [20] Liao PF & Wokaun A (1982) Lightning rod effect in surface enhanced Raman scattering. *The Journal of Chemical Physics* 76(1):751-752.
- [21] Moskovits M (1985) Surface-enhanced spectroscopy. *Reviews of Modern Physics* 57(3):783-826.
- [22] Champion A & Kambhampati P (1998) Surface-enhanced Raman scattering. *Chemical Society Reviews* 27(4):241-250.
- [23] Kneipp K, et al. (1997) Single Molecule Detection Using Surface-Enhanced Raman Scattering (SERS). *Physical Review Letters* 78(9):1667-1670.
- [24] Graham D, Mallinder BJ, & Smith WE (2000) Surface-Enhanced Resonance Raman Scattering as a Novel Method of DNA Discrimination. *Angewandte Chemie International Edition* 39(6):1061-1063.
- [25] Podstawka E, Ozaki Y, & Proniewicz LM (2004) Part I: Surface-Enhanced Raman Spectroscopy Investigation of Amino Acids and Their Homodipeptides Adsorbed on Colloidal Silver. *Appl. Spectrosc.* 58(5):570-580.
- [26] Otto A, Mrozek I, Grabhorn H, & Akemann W (1992) Surface-enhanced Raman scattering. *Journal of Physics: Condensed Matter* 4(5):1143.
- [27] R. Aroca SEVS, Wiley, West Sussex, 2006.
- [28] P. P. Edwards RLJCNRRiMCiC, P.Braunstein, L.A.& OroPRRE, Wiley VCH, Weinheim (1999)
- [29] Collier CP, Vossmeier T, & Heath JR (1998) NANOCRYSTAL SUPERLATTICES. *Annual Review of Physical Chemistry* 49(1):371-404.

## Chapter 1

---

- [30] Nanoparticles and Nanostructured Films” EJHF, Wiley-Vch, Weinheim, (1998)
- [31] Pietron JJ, Hicks JF, & Murray RW (1999) Using Electrons Stored on Quantized Capacitors in Electron Transfer Reactions. *Journal of the American Chemical Society* 121(23):5565-5570.
- [32] Anonymous (L. W. MCKEEHAN ) The Molecular Field and Atomic Order in Ferromagnetic Crystals and in Hydrogenised Iron. *nature* 126:952-953.
- [33] E.C. Stoner EPW, *Proc. Phys. Soc. A*, 240, 599, (1948)
- [34] Holz A & Scherer C (1994) Topological theory of magnetism in nanostructured ferromagnets. *Physical Review B* 50(9):6209-6232.
- [35] Guozhong Cao NNS, *Properties and Applications*, Imperial College Press, London, 2004, pp.382

## Synthesis of corrugated pentagonal bipyramidal Au microstructures ( $\mu$ -CPBs) and their applications in SERS

### Summary

This chapter deals with the synthesis of Au  $\mu$ -CPBs, growth and their applications in SERS. Au  $\mu$ -CPBs have been prepared by a simple solid state reaction. A metal-organic precursor (termed as AuAg-ToABr) prepared by the phase transfer of Au(III) and Ag(I) ions to the organic phase using tetraoctylammonium bromide, was subjected to thermolysis at 135 °C for 12 hrs in air. The obtained microstructures have pentagonal bipyramidal symmetry with lengths beyond  $\sim 10$   $\mu\text{m}$  and central widths 0.9 - 1.15  $\mu\text{m}$ , while the tips are few tens of nanometers. Here, Ag(I) only guides the microstructure and does not become part of it. Thus,  $\mu$ -CPBs are essentially made of Au. It is possible to vary their size based on the thermolysis time, temperature and the Au(III):Ag(I) ratio. The  $\mu$ -CPBs are found to enhance the Raman signal of molecules chemisorbed on the surface, particularly at the tips where the electric field is high. The efficiency of the  $\mu$ -CPBs tips is demonstrated in a *prick and probe* experiment.

---

Manuscript based on this work is under preparation

### 2.1 Introduction

Synthesis of metal nanoparticles has attracted wide attention in recent years, owing to their versatile applications in catalysis [1], plasmonics [2], surface-enhanced Raman scattering (SERS) [3-6], imaging [7], and sensors [8-10]. Au and Ag nanoparticles have been extensively studied due to the tunable morphology and thereby the optical response [11]. Among all the possible nanoparticle morphologies, one-dimensional nanostructures like nanorods, nanowires and bipyramids have attracted significant interest due to their highly tunable localized surface plasmon resonance (LSPR). For instance, Au nanorods optical absorption can be tuned from visible to near infrared region as a function of the particle aspect ratio [12]. The Au nanorods with a pentagonal base and sharp apexes would lead to Au bipyramidal structures. Bipyramidal nanostructures are often called nanorice in literature. Both nanorods and bipyramids have two surface plasmon resonances namely transverse and longitudinal modes which arise due to the electron oscillations along the longitudinal and transverse directions. Since Au bipyramid tips are sharper than those of nanorods, the electric field enhancement is expected to be more at the tip of the Au bipyramids according to the lightning-rod effect. Due to this reason, Au bipyramids could be potential candidates for SERS [13]. Additionally, Au bipyramids were also exploited in varied applications such as studying the damping in the acoustic vibrations [14], CO oxidation [15] etc. Odom and co-workers have shown the photothermal response of the Au nanopyramids with sharp tips [16]. Au nanorice/bipyramids have been used in dielectric sensing [17]. The sensitivity is found to increase as the size and the aspect ratio of the Au bipyramids is increased [18]. A literature survey of length of bipyramids/nanorice is presented in Table 2.1.

The existing reports in the literature for the synthesis of Au bipyramids are seed-mediated and are multistep reactions [19]. Other disadvantages include usage of high concentration of surfactants to control the growth [18], highly acidic conditions [14] and long reaction times [15] etc. These methods generally produce nanorice/bipyramids having rounded tips.

Table 2.1: Literature reports for the synthesis of Au rice/pentagonal bipyramidal structures ( $\mu$ -CPBs).

S.No	Shape	Approximate length (nm)	Reference
1	Au bipyramids, 3D particles	75	[20]
2	Au bipyramids, 3D particles	100	[21]
3	Au/Ag alloy bipyramids, 3D particles	40-90	[22]
4	Au bipyramids, 3D particles	200	[13]
5	Au bipyramids, 3D particles	75	[14]
6	Au bipyramids, 3D particles	100	[23]
7	Au bipyramids, 3D particles	250-350	[19]
8	Au bipyramids, 3D particles	100	[17]
9	Ag nanorice	450	[24]
10	Au bipyramids, 3D particles	600	[25]
11	Au bipyramids, 3D particles	130	[18]
12	Au bipyramids, 3D particles	100	[26]
13	Au bipyramids, branched Au structures	70	[27]
14	Au nanorice	50-70	[15]
15	Au nanorice	370	[28]
16	Fe <sub>2</sub> O <sub>3</sub> /Au core shell bipyramidal structures	400	[29]
17	Au bipyramids	100	[30]
18	Au bipyramids	100	[31]
19	Au bipyramids	55	[32]

Besides chemical methods, lithography based methods have also been employed to produce metal anisotropic structures. Metal wires with sharp tips produced by lithography are most sought after in plasmonic waveguides [33]. However, lithography based method involve prefabricated templates, focused ion beam (FIB) milling, metal deposition, template stripping and such processes [34-38] and are not practical for large scale synthesis.

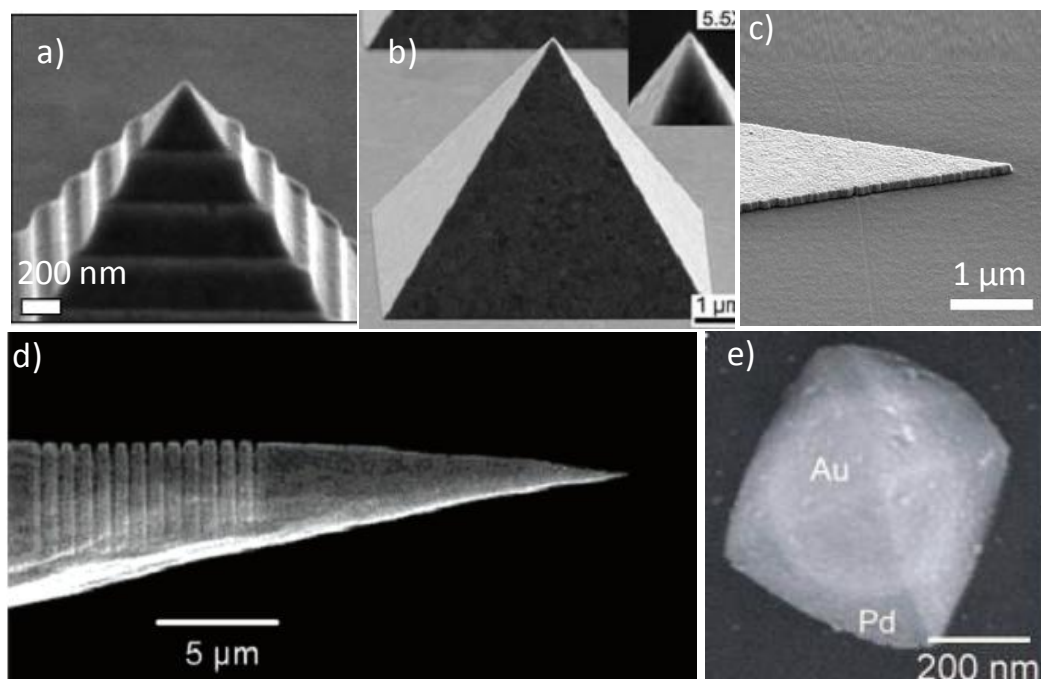


**Figure 2.1** Fabrication of sharp metal tips (metal anisotropic structures) has been done using various lithography techniques [From ref. 34-38].

### 2.2 Scope of the investigation

As seen from the comprehensive survey in Table 1, the longest rice/bipyramids reported in the literature are  $\sim 0.6 \mu\text{m}$ . These methods involve multistep, seed mediated routes. The product in general, contains unwanted species such as 3D anisotropic structures, chemical residues etc. On the other hand, lithography based methods are clean but are obviously expensive and time consuming. This chapter deals with a simple method of producing Au  $\mu$ -corrugated pentagonal bipyramids ( $\mu$ -CPBs) in high yield, with lengths beyond  $10 \mu\text{m}$  while tips being sharp (tip diameter  $< 50 \text{ nm}$ ).

### 2.3 Experimental details

Hydrogen tetrachloroaurate(III) hydrate ( $\text{HAuCl}_4 \cdot 3\text{H}_2\text{O}$ ), silver nitrate ( $\text{AgNO}_3$ ), tetraoctylammonium bromide (ToABr), and toluene were obtained from Sigma Aldrich and used without further purification. The water used throughout this investigation was double distilled and deionized. To a 1.5 mL of  $\text{HAuCl}_4$  (25 mM), 6 mL of tetraoctylammonium bromide (ToABr) in toluene (50 mM) was added and stirred for 5 min. The bottom aqueous phase became colorless and top organic phase developed red color. Then, a 0.5 mL of  $\text{AgNO}_3$  (25 mM) was added to the solution and stirred for  $\sim 10$  hrs. The resultant organic phase was in red color as shown in Figure 2.2. In this

case, the volume ratio of Au(III) and Ag(I) in aqueous phase was 75:25. Likewise, different volume ratios of Au(III) and Ag(I) such as 50:50, 65:35, 80:20, 90:10 have been prepared. In all the experiments, the volume ratio of aqueous and organic phase was kept constant as 1:3. The substrates used i.e., Si and glass were cleaned twice with water, IPA, toluene and dried under  $N_2$  gas.

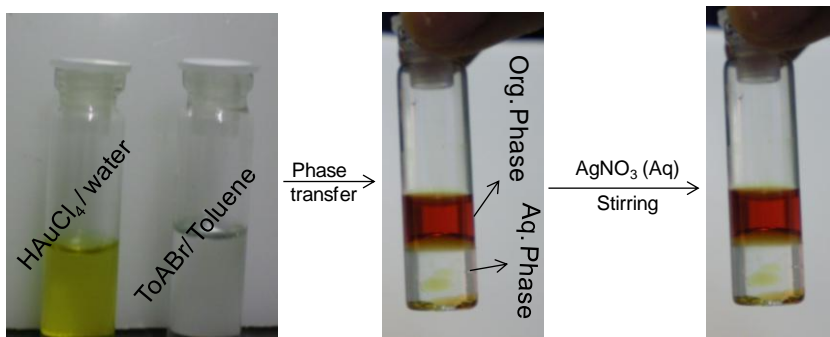


**Figure 2.2** Steps involved in the precursor preparation.

## 2.4 Results and discussion

The phase transferred organic phase (henceforth termed as AuAg-ToABr) was separated using a micropipette. After the evaporation of solvent, the isolated solid precursor was characterized using IR spectroscopy, XRD and TGA.

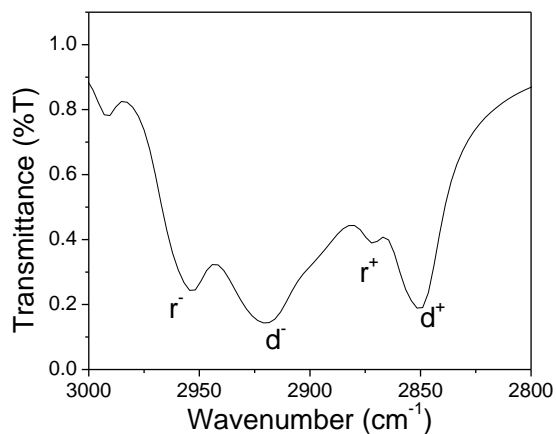


**Figure 2.3** IR spectrum obtained from the solid precursor, in the region of C-H stretching.

In the IR spectrum (Figure 2.3), the peaks at 2952 and 2870  $cm^{-1}$  correspond to asymmetrical and symmetrical vibrational modes of  $CH_3$ , respectively. The peaks at 2924 and 2850  $cm^{-1}$  refer to asymmetrical and symmetrical vibrational modes of  $CH_2$ , respectively. The IR data shows the presence of ToABr organic component in the precursor. The precursor solid was further characterized using XRD (Figure 2.4). It shows that precursor crystallizes in a lamellar structure and there are peaks

assignable to ToABr, Au-ToABr and Ag-ToABr, perhaps existing in separate domains. This will be discussed in detail in the section 2.4.

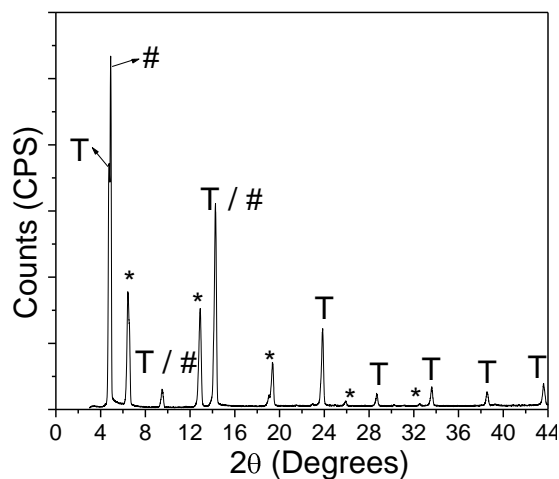


**Figure 2.4** XRD pattern collected from AuAg-ToABr film made by solvent evaporation at the room temperature. Here, T=ToABr, \*=Au ToABr, #=Ag ToABr.

### 2.4.a Synthesis and characterization of $\mu$ -CPBs

The  $\mu$ -CPBs were prepared on Si and glass substrates. The AuAg-ToABr in toluene (~10 mM) was drop coated on Si or glass substrates and thermolyzed at 135 °C for 12 hrs. Following thermolysis, the substrates were washed with toluene to remove any unreacted precursor. These steps are illustrated in Figure 2.5

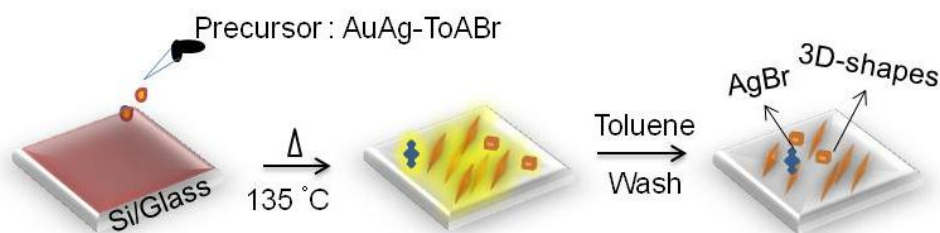


**Figure 2.5** Schematic illustrating the synthetic procedure of  $\mu$ -CPBs.

At this stage, the sample is characterized using XRD, FESEM and EDS. The XRD data shown in Figure 2.6a, contained peaks due to AgBr and metallic Au (metallic Ag and AgAu alloy, if present would not show up separately as their peaks would be very close to the peaks due to Au). Micrometer ( $\mu$ m) size AgBr structures along with Au particles were observed (see Figure 2.6b). It appears that Ag(I) prefers AgBr over metallic Ag. The EDS supports the presence of Au, Ag and Br (see Figure 2.6b). These observations collectively point out that the thermolyzed product consists of



metallic Au and AgBr. Since the reduction potential of  $\text{AuCl}_4^-/\text{Au}$  (1 V) is higher than the  $\text{AgBr}_2^-/\text{Ag}$  (< 0.8 V), Au(III) reduces to metallic Au whereas  $(\text{AgBr}_2)^-$  forms AgBr precipitate [39].

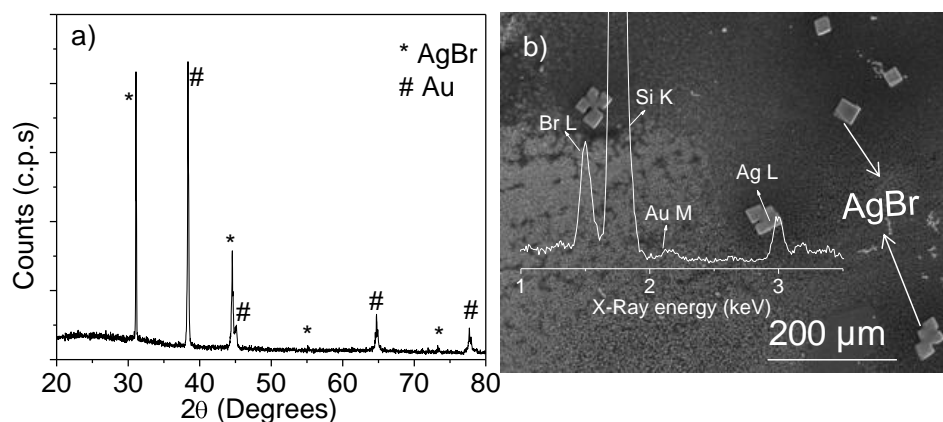


**Figure 2.6** (a) XRD pattern collected from the sample just after washing with toluene. (b) Low magnification FESEM image shows  $\mu\text{m}$  size AgBr crystals indicated by arrow. EDS spectrum from the sample is overlaid.

In TGA, the decomposition of the AuAg-ToABr precursor started at  $\sim 160^\circ\text{C}$  as shown in Figure 2.7. The weight loss in TGA occurs in three steps - region I (20.46%), regions II (53.61%) and region III (12.31%) correspond respectively to the solvent evaporation, decomposition, and desorption of ToABr, ToA, and chloride ions, and the metallic residue. The residue was 13.6 wt% which is a composed of metallic Au and AgBr (supported by Figure 2.6). Based on TGA, the derived formula is  $(\text{AuCl}_4)^-(\text{AgCl}_2)^-.4\text{ToABr}$ , which in a simplified way, is written as AuAg-ToABr.

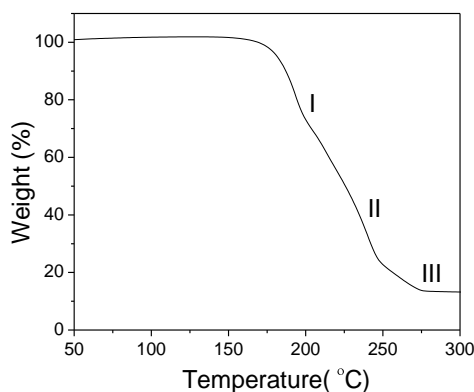


**Figure 2.7** TGA of the precursor showing various stages (I-III) during the decomposition of AuAg-ToABr.

## Chapter 3

In order to remove the AgBr crystals, the thermolyzed product was washed with conc.  $\text{NH}_3$  (see Figure 2.8). The resulting solid was examined using FESEM, EDS, UV/vis/NIR absorption spectroscopy, XRD and HRTEM.

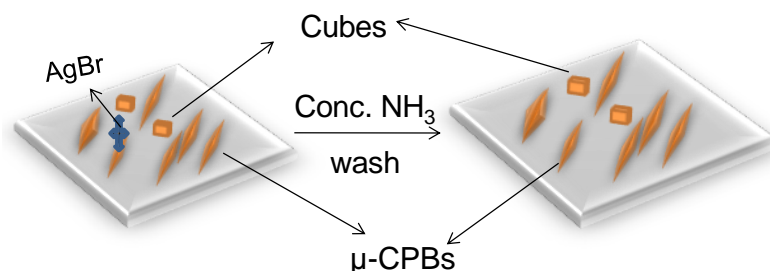


**Figure 2.8** Schematic illustrating the removal of AgBr.

FESEM images of Au  $\mu$ -CPBs at different magnifications have shown in Figure 2.9. Cubes and decahedron are also observed along with  $\mu$ -CPBs. The length of  $\mu$ -CPBs ranges from 10 - 12  $\mu\text{m}$  (average, 11  $\mu\text{m}$ ) with a thickness, 0.9 - 1.15  $\mu\text{m}$  (average, 1  $\mu\text{m}$ ), as shown in the Figure 2.9a. High magnification imaging of  $\mu$ -CPBs showed clearly the presence of corrugated surface with tips of few tens of nms (Figure 2.9b and c). It appears that the corrugated structure carries a fivefold symmetry (Figure 2.9d).

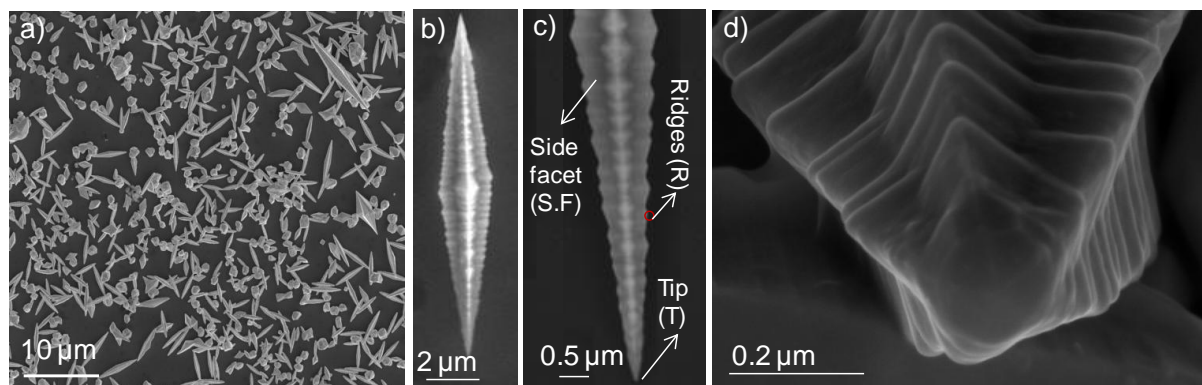


**Figure 2.9** (a-c) FESEM images of  $\mu$ -CPBs at different magnifications and d) Cross section view of the  $\mu$ -CPBs obtained on tilting by the sample at  $60^\circ$ .

Owing to their large size, Au  $\mu$ -CPBs may be observed under a normal optical microscope as well (Figure 2.10). Neither Ag nor Br is observed in EDS mapping (see Figure 2.11), as these are purely composed of Au.

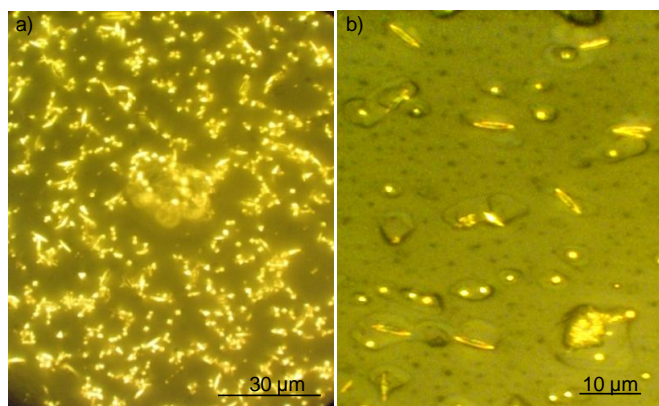


**Figure 2.10** Optical microscopy images of  $\mu$ -CPBs at different magnifications.

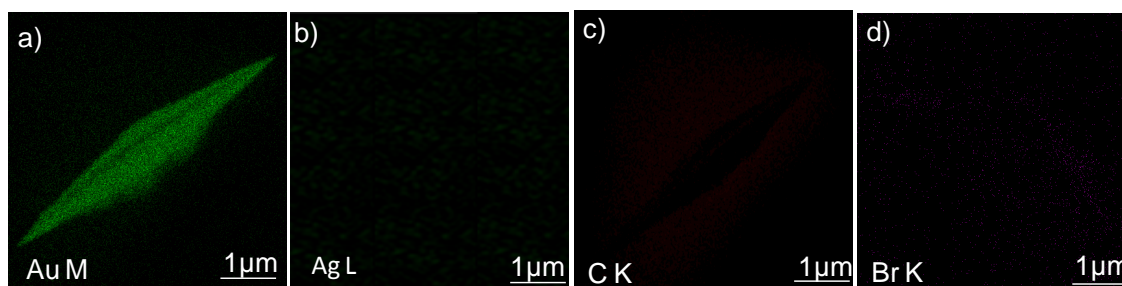


**Figure 2.11** EDS mapping of single  $\mu$ -CPBs for Au M, Ag L, C K and Br K level.

From an earlier report from this laboratory, it is known that Au-ToABr alone, in the absence of Ag-ToABr, gives rise to micron sized polygonal plate like structures of Au [40, 41]. Thus, Au  $\mu$ -CPBs are observed only in the presence of Ag(I). But EDS data in Figure 2.11 does not show any Ag. Since the theoretical detection limitation of EDS is  $\sim 0.15$  at% [42],  $\mu$ -CPBs were further examined using XPS (Figure 2.12). As shown in Figure 2.12b, the Au 4f core-level region shows two peaks at  $\sim 84.18$  and  $\sim 87.80$  eV corresponding to  $4f_{7/2}$  and  $4f_{5/2}$  levels, respectively [43]. In the Ag 3d spectral range (Figure 2.12c), two peaks were seen with mild intensity, at  $\sim 368.04$  and  $\sim 373.98$  eV assignable to  $3d_{5/2}$  and  $3d_{3/2}$ , respectively [44]. These two peaks can be attributed to the presence of Ag(0). No peaks were detected in the Br 3d spectral range of  $\sim 68 - 70$  eV (Figure 2.12d) [44]. From the XPS data, the mole fraction of Ag on Au  $\mu$ -CPBs is estimated to be  $\sim 4\%$ .

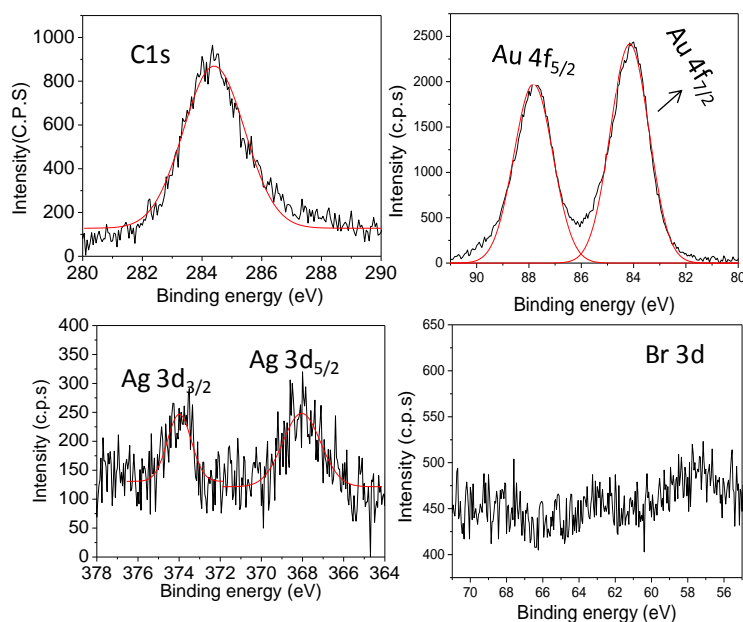


**Figure 2.12** Core level spectra in the regions of C1s, Au 4f, Ag 3d and Br 3d. The C1s (284.4 eV) signal was used for energy calibration.

UV/vis/NIR absorption spectrum of the  $\mu$ -CPBs particles on a glass substrate shows two absorption peaks at  $\sim 608$  and  $\sim 988$  nm (Figure 2.13). From the literature reports on Au anisotropic nanostructures, these peaks should correspond respectively to transverse and longitudinal surface plasmons modes [45]. The first peak was red-shifted by  $\sim 58$  nm compared to nanorods of same dimension ( $\sim 550$  nm), due to the ridges like structures along the  $\mu$ -CPBs [19]. The longitudinal mode ( $\sim 988$  nm) was observed to be broadened at higher wavelengths, due to the distribution in the length of the  $\mu$ -CPBs as well as due to contributions from other shaped particles.

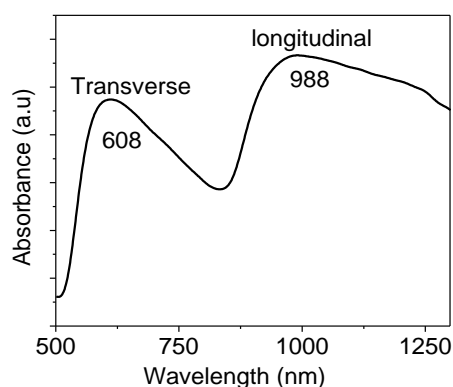


**Figure 2.13** UV/vis/NIR absorption spectrum of Au  $\mu$ -CPBs.

XRD pattern collected from the  $\mu$ -CPBs (Figure 2.14) shows the highly crystalline nature of the  $\mu$ -CPBs. The table shown alongside gives a comparison between polycrystalline bulk Au (JCPDS Pdf #65-2870) and Au  $\mu$ -CPBs. The intensity of the (220) peak is somewhat higher due to preferred orientation of  $\mu$ -CPBs (*vide infra*).

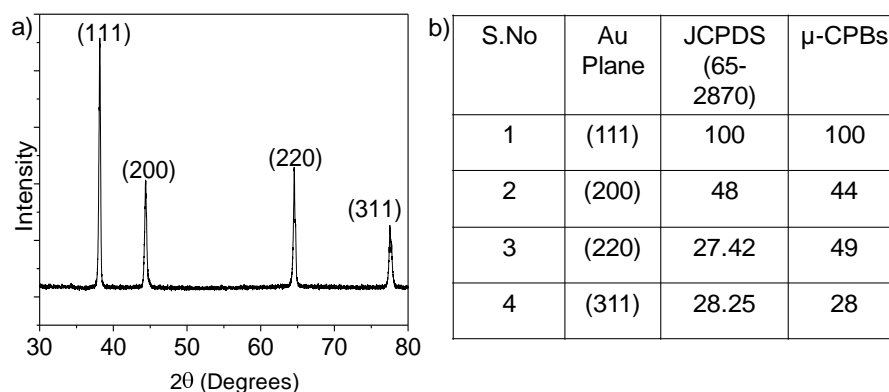


**Figure 2.14** a) XRD pattern collected from the  $\mu$ -CPBs, b) Comparison of relative intensities of XRD peaks of  $\mu$ -CPBs with polycrystalline Au JCPDS data (65-7820).

In order to understand the structure of the  $\mu$ -CPBs in detail, high resolution SEM and TEM analysis have been performed. Figure 2.15a shows highly magnified SEM image of a  $\mu$ -CPB with various planes and growth direction assigned, based on ED analysis. Figure 2.15c shows an ED pattern collected from the tip of the  $\mu$ -CPB. Two EDs, one hexagonally symmetric and another parallelepiped were observed overlapping each other. These correspond to a Au FCC lattice viewed along the  $\langle 111 \rangle$  and  $\langle 110 \rangle$  zone axes, respectively. The ED pattern from the centre of  $\mu$ -CPB also shows two sets of spots indexable to  $\langle 112 \rangle$  and  $\langle 001 \rangle$  zone axes as shown in Figure 2.15e. Murphy and coworkers also observed similar EDs for penta-twinned nanorods [46]. This indicates that the  $\mu$ -CPBs possess a penta-twinned structure grown along the  $\langle 110 \rangle$  direction [46]. ED pattern collected from the side parts of the  $\mu$ -CPBs is assigned for  $\langle 111 \rangle$  zone axis (Figure h and j).

When HRTEM was performed at the tip, the observed spacing between the fringes was  $\sim 2.36$  Å corresponding to a  $d$ -spacing of Au(111) (Figure 2.15d). Figure 2.15(f-g,i and k) are HRTEM images collected from the various regions of the side facets of  $\mu$ -CPBs. In all the regions, the  $d$ -spacing was  $\sim 2.06$  Å corresponding to Au(200). Based on the above results, the growth direction of the  $\mu$ -CPBs is considered to be  $\langle 110 \rangle$  while  $\mu$ -CPBs side facets are  $\{100\}$  and the tips are enclosed with stable  $\{111\}$  facets, in agreement with the reported literature of Au nanorice crystal structure [13, 21, 22, 47].

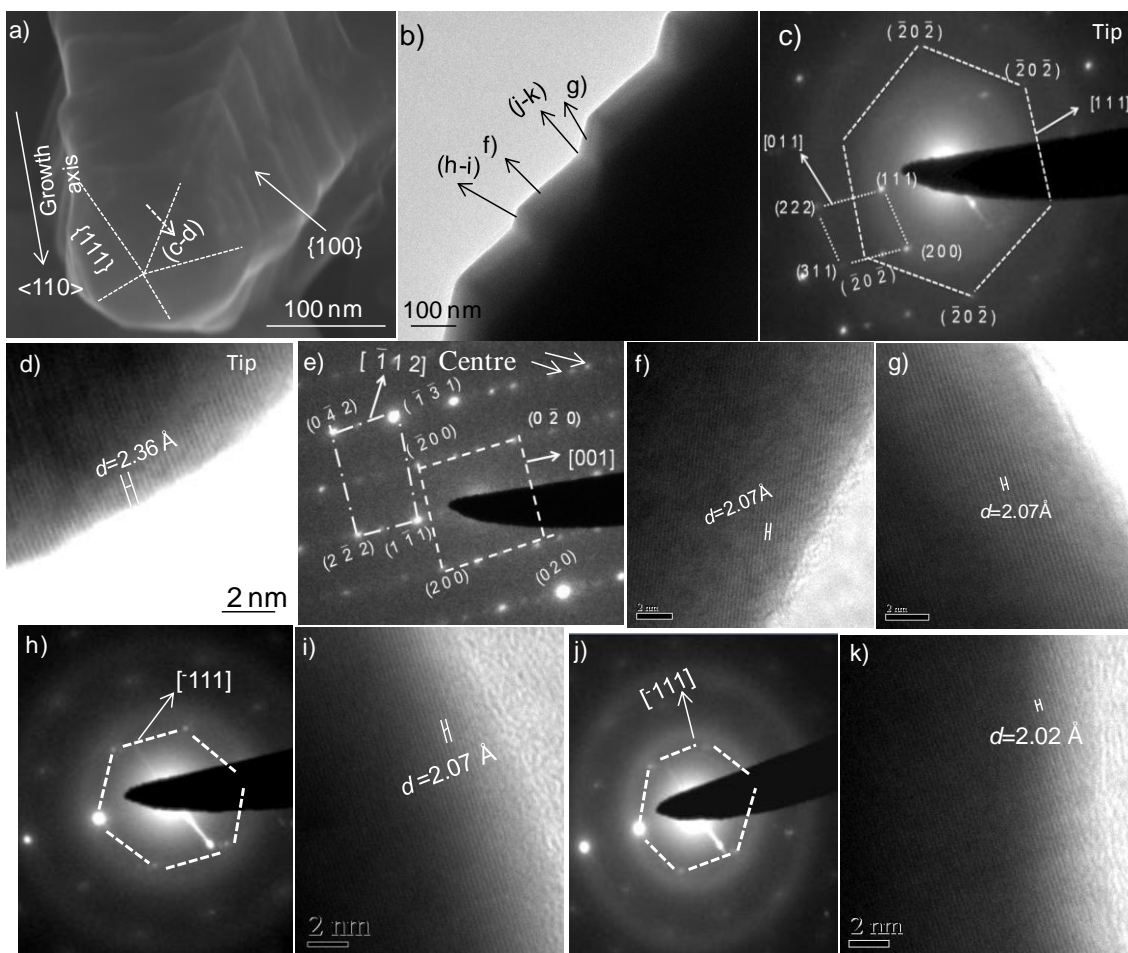


**Figure 2.15** a) A high magnification FESEM image of a single  $\mu$ -CPB, oriented in  $\langle 110 \rangle$  direction with indexed side facets. b) Low magnified TEM image of  $\mu$ -CPB showing periodic corrugated ridges. (c-d) ED and HRTEM collected from the tip of the  $\mu$ -CPBs,  $d = 2.36 \text{ \AA}$  corresponding to Au(111) plane. e) ED pattern from the centre of the  $\mu$ -CPBs. (f-k) HRTEM and ED patterns collected from the side facets of the  $\mu$ -CPBs,  $d \sim 2.06 \text{ \AA}$  corresponding to Au(200) plane.

The  $\mu$ -CPBs (shown in Figure 2.9) were obtained by optimizing the synthetic conditions such as the ratio of  $\text{HAuCl}_4$  and  $\text{AgNO}_3$  in the precursor and the thermolysis temperature. Figure 2.16 shows FESEM images of  $\mu$ -CPBs prepared with different volume ratios of  $\text{HAuCl}_4$  and  $\text{AgNO}_3$  at  $135^\circ\text{C}$ . As the  $\text{HAuCl}_4$  volume increases,  $\mu$ -CPBs particles grew longer and also developed faceted structures on the surface. As the volume ratio of  $\text{Au(III):Ag(I)} = 75:25$  produced long  $\mu$ -CPBs with good yield, further fine variations in the volume ratio were done below and above 75:25. The periodicity of the ridges present on the  $\mu$ -CPBs decreased as the volume ratio was varied from 72:28 to 78:22. When  $\text{HAuCl}_4$  became more than 80%, the  $\mu$ -CPBs were relatively shorter and the surface

corrugation reduced. At 90:10, short drum shaped particles, distinctly different from  $\mu$ -CPBs, were obtained along with other polyhedral structures as shown in Figure 2.16.

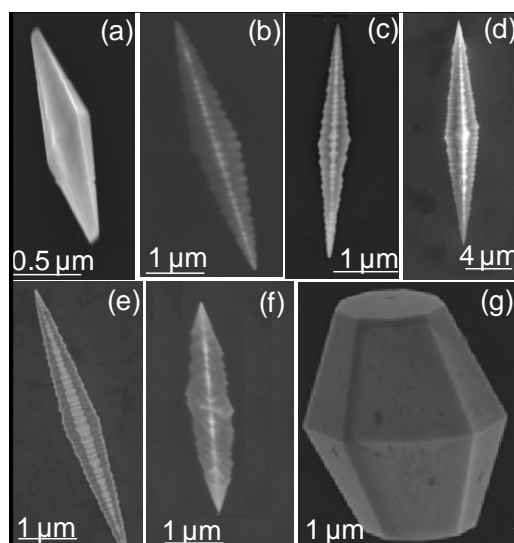


**Figure 2.16** Magnified FESEM images of  $\mu$ -CPBs prepared at 135 °C with varying volume ratio of  $\text{HAuCl}_4$  (25mM) and  $\text{AgNO}_3$ (25mM), (a) 50:50, (b) 65:35, (c) 72:28, (d) 75:25, (e) 78:22, (f) 80:20 and (g) 90:10.

Thermolysis at 250 °C produced small  $\mu$ -CPBs with no corrugations. Although all the ratios gave  $\mu$ -CPBs, among them, 75:25 ratio of  $\text{HAuCl}_4$  and  $\text{AgNO}_3$  yielded higher proportion of  $\mu$ -CPBs. Other volume ratios, 50:50, 80:20 and 90:10 produced more of other polyhedral shapes such as cubes, decahedrons etc.

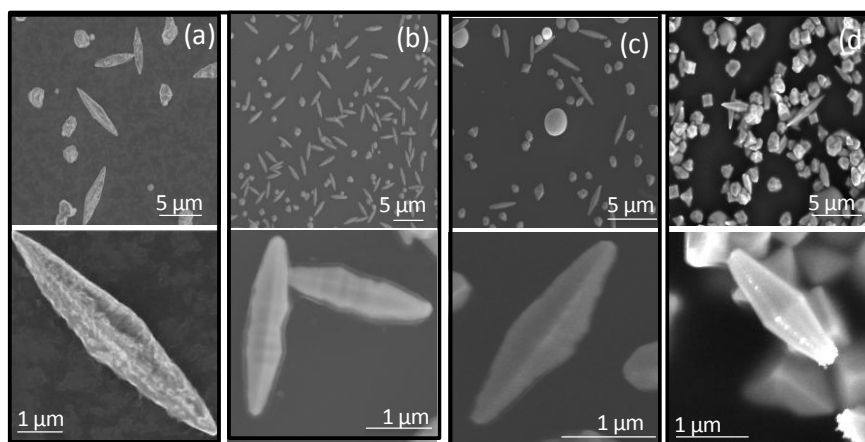


**Figure 2.17** FESEM images of  $\mu$ -CPBs prepared at 250 °C with varying volume ratio of  $\text{HAuCl}_4$  (25mM) and  $\text{AgNO}_3$  (25 mM), (a) 50:50, (b) 75:25, (c) 80:20 and (d) 90:10. The corresponding magnified images are shown below.

## Chapter 3

---

Apart from surface corrugations and yield of  $\mu$ -CPBs, volume ratio has a considerable effect on the size of the  $\mu$ -CPBs as well. The ratio of 50:50 gave  $\sim 5.8 \mu\text{m}$  long  $\mu$ -CPBs whereas 75:25, 80:20 and 90:10 produced  $\mu$ -CPBs with average lengths of  $\sim 5$ , 3.2 and  $1.5 \mu\text{m}$  respectively as shown in Figure 2.17. Other important growth parameter is the temperature of thermolysis. When the thermolysis was carried out at various temperatures, the morphology as well as the size of the  $\mu$ -CPBs varies. Keeping the ratio of  $\text{HAuCl}_4$  and  $\text{AgNO}_3$  at 75:25, growth temperature of  $\mu$ -CPBs is varied from  $135^\circ\text{C}$  to  $250^\circ\text{C}$ . Below  $135^\circ\text{C}$  growth temperature, the precursor did not decompose. This goes well with the TGA of the precursor, which indicates that there is no weight loss below  $135^\circ\text{C}$ . The  $\mu$ -CPBs formed at  $135^\circ\text{C}$  and  $155^\circ\text{C}$  were sharp and long, whereas the ones prepared at  $175^\circ\text{C}$  were smooth pentagonal bipyramids.

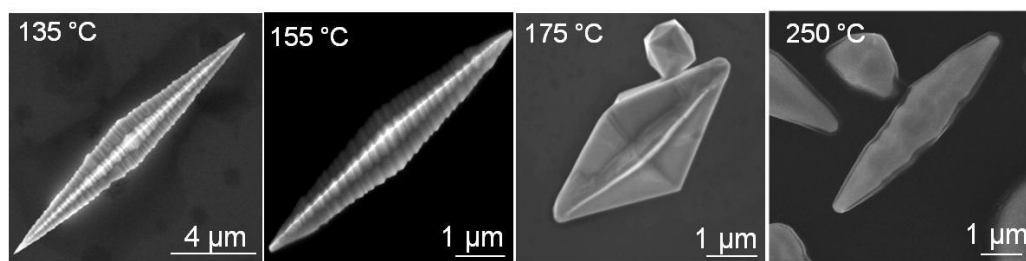


**Figure 2.18** FESEM images of  $\mu$ -CPBs obtained at various temperature of thermolysis.

As the temperature increases,  $\mu$ -CPBs length as well as surface structures decreased drastically as shown in Figure 2.18.  $\mu$ -CPBs prepared at  $250^\circ\text{C}$  possess relatively smoother surfaces and resemble the reported nanorice morphology in the literature [27]. At higher growth temperatures such as  $150^\circ\text{C}$ ,  $175^\circ\text{C}$  and  $250^\circ\text{C}$ , the higher growth kinetics does not permit corrugated structure formation and thus we observe only smooth surfaces. Also, faster kinetics of reduction at higher temperature ( $250^\circ\text{C}$ ) leads to a large number of the nucleation sites and in turn higher number of short  $\mu$ -CPBs ( $\sim 4 \mu\text{m}$ ).

The above results are shown in the form of a histogram (Figure 2.19). It is clear that the optimal conditions are 75:25 of Au:Ag and thermolysis at  $135^\circ\text{C}$  where the long  $\mu$ -CPBs were obtained with a maximum yield of 60%. At all the growth temperatures above  $135^\circ\text{C}$  (at 75:25 of Au(III) and Ag(I)), the yield of the  $\mu$ -CPBs was  $> 45\%$  typically following the trend as shown in the histogram in Figure 2.19b. The  $\mu$ -CPBs presented above are clearly distinct from the reports in the literature. The latter were small in size with smooth surfaces and generally cannot be observed using



conventional optical microscope. All those are classified as nanorice. The  $\mu$ -CPBs presented here carry ridges and highly periodic facets and therefore differs much from the nanorice particles.

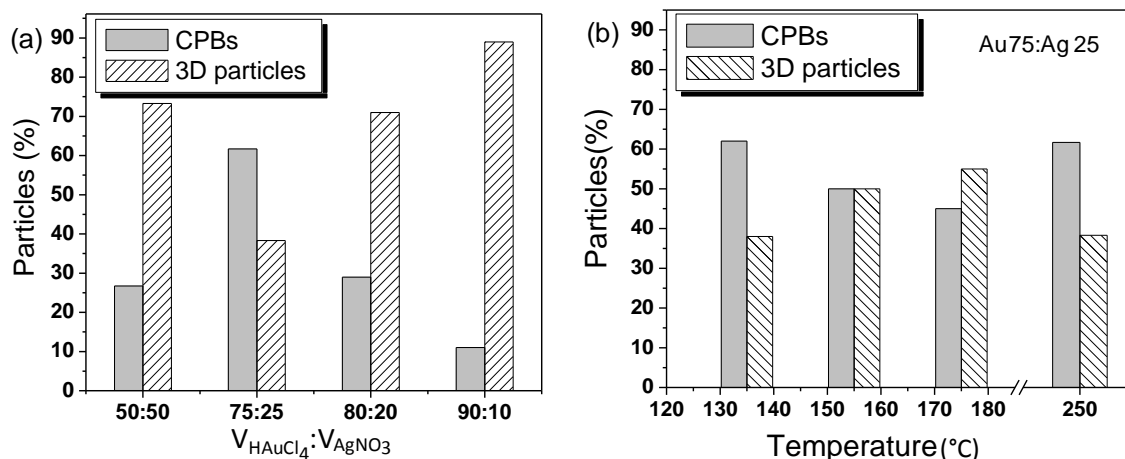


**Figure 2.19** Histograms showing the relative populations of  $\mu$ -CPBs particles and 3D particles for different (a) volume ratios of  $\text{HAuCl}_4$  and  $\text{AgNO}_3$ , (both at 25 mM) thermolyzed at  $250^\circ\text{C}$  (b) Thermolysis temperatures (at  $\text{HAuCl}_4 : \text{AgNO}_3$  of 75:25).

As mentioned previously (see Figure 2.6), the thermolyzed product apart from  $\mu$ -CPBs, contained AgBr crystals which were washed away using conc  $\text{NH}_3$ , (Figure 2.20a), the presence of excess silver (besides AgBr) peaked at 75:25 volume ratio of Au(III) and Ag(I), and interestingly, at this ratio, well formed long CPBs have been observed. The excess Ag decreased on either side and for 50:50, 80:20 and 90:10 volume ratios of Au(III)/Ag(I), there was no predictable amount of metallic Ag. Figure 2.20b shows the at% of Au, Ag and Br in the thermolyzed product for all the volume ratios employed. It is clearly evident that the amount of Ag exceeds Br prominently at 75:25 of Au(III) and Ag(I) ratio. For 10, 20, 50 volumes of Ag(I) the at% of Br is higher than the at% of Ag, and thus there is no excess silver here which can be considered as metallic Ag. For the intermediate volume ratios (22, 25, 28) of Ag(I), Br at% is lesser than the Ag at%. It gives indirect evidence that presence of Ag/AgBr is crucial to construct  $\mu$ -CPBs.

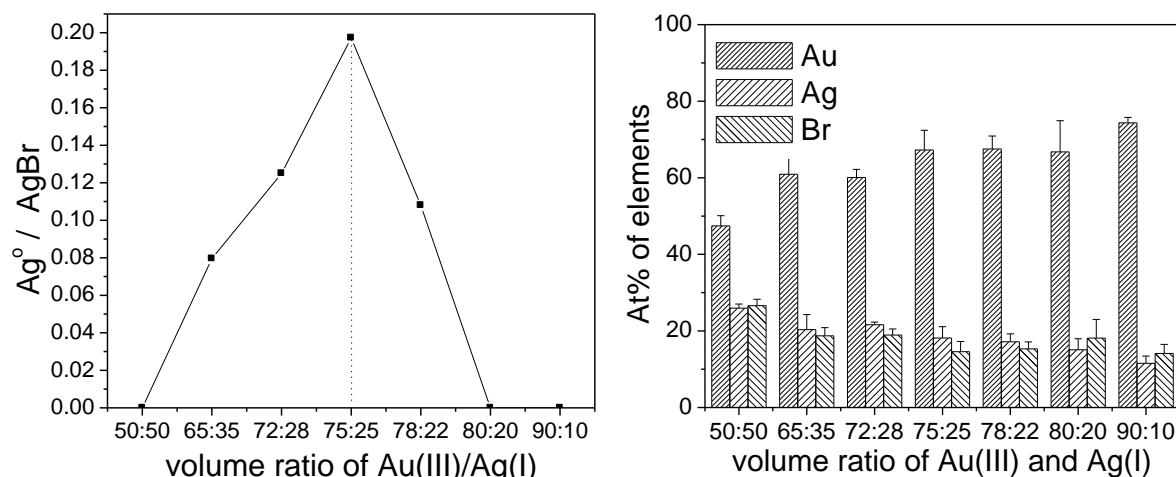


**Figure 2.20** (a) Plot illustrating the presence of excess metallic Ag for the volume ratio of 75:25 of Ag(I) and Au(III) respectively, All the volume ratios of Au(III) and Ag(I) were thermolyzed at 250 °C for 1 hr and EDS was collected from the each sample over different areas and averaged. (b) Histogram showing the at% of Au, Ag and Br as a function of the volume ratio of the Au(III) and Ag(I).

#### 2.4.b Growth mechanism of $\mu$ -CPBs

The growth of  $\mu$ -CPBs is indeed interesting. It has two growth modes- along the longitudinal axis and along the lateral growth leading to the observed corrugation (five-fold stars stacked along the longitudinal growth direction). This aspect investigated by carrying out FESEM measurements on substrates by arresting the growth at different time periods by simply removing the substrate from the hot plate. As seen from Figure 2.22, the thermolysis carried out for 30 min gives rise to nearly spherical particles in the range, 25 - 30 nm. They may have definite facets which is however not clearly visible in the FESEM images. The facets become visible when the particles grew beyond 100 nm (time of thermolysis, 60 min). This is essentially a decahedron which is one among the known stable polyhedron in this size regime [48]. Decahedron can act as a seed for further growth. It has ten  $\{111\}$  facets, five  $\{100\}$  facets and two possible growth directions,  $\langle 110 \rangle$  is along the particle axis and five equivalent  $\langle 112 \rangle$  directions across the particle side faces as shown in Figure 2.21 [49]. Anisotropic particles growth is mainly based on the differences in the growth rates on different crystallographic facets. For FCC metals, the surface energy  $\gamma$  of different facets is as follows –  $\gamma_{\{111\}} < \gamma_{\{100\}} < \gamma_{\{110\}}$ . The  $\{110\}$  and  $\{211\}$  faces have surface energies of 0.0991 and 0.0908 eV/Å<sup>-2</sup> respectively [50]. Hence the faster growth along the  $\langle 110 \rangle$  direction is understandable. The growth rate along the  $\langle 112 \rangle$  direction comes next [49].

*Growth along the  $\langle 112 \rangle$  direction:* Decahedron considered as assembly of five tetrahedral units, sharing a common edge. The angle expected between two tetrahedral units is  $70.53^\circ$ . When five such tetrahedrons are stacked in a face to face orientation, there will be an angular gap of  $7.35^\circ$  to fill in [51]. It therefore causes some strain at the boundary [45]. The boundary thus acts as a reactive site to generate ridges-like extra growths on the decahedron. As shown in Figure 2.21, the twin planes are oriented in the  $\langle 112 \rangle$  direction. Ag preferentially deposits on the Au{100} facets due to its lower deposition potential. On this plane, Ag finds higher coordination than on Au{111} [21]. Ag present in between the twin planes on Au{100} facets could be oxidized by a bromide ion present in the reaction mixture, leading to discharge of an electron [15]. The role of the electron will be explained in the next paragraph. Instead, Ag present at the twin planes gets galvanically displaced by Au(I) and thus stabilizes the energetic twin plane [52]. This could be the mechanism for the growth of a star shape from a decahedron. Ag deposition, dissolution and galvanic displacement of Au happens repeatedly to produce a well defined star shape from a decahedron base [53]. These ridges are (100) planes as shown in the TEM analysis. Figure 2.21 represents the growth mechanism along the  $\langle 112 \rangle$  direction. The ridges along the  $\langle 112 \rangle$  directions are the corrugated structures from the top view of the  $\mu$ -CPBs.

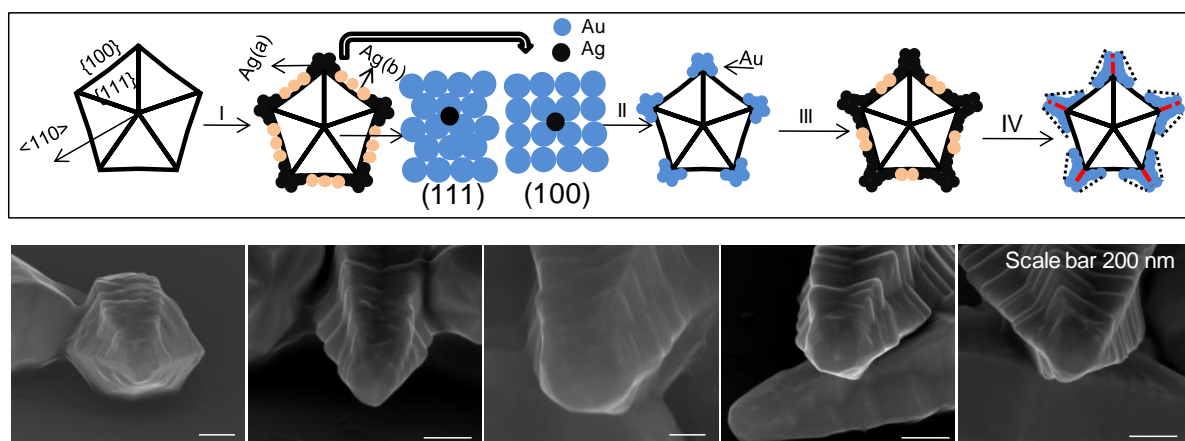


**Figure 2.21** Schematic illustrating the growth mechanism of the  $\mu$ -CPBs along the  $\langle 112 \rangle$ . Ag(I) deposition on Au{100} facets and Ag(0) is galvanic displaced by Au(I). This process repeated to lead fivefold star along the  $\langle 110 \rangle$ . FESEM from various particles supports the above mechanism.

*Growth of the decahedron along the  $\langle 110 \rangle$  direction:* Multiple twinned decahedrons are the seed to obtain  $\mu$ -CPBs. Nanoparticles obtained at 90 min thermolysis appear like elongated decahedrons. They are addressed as nanorice, with typical length of  $\sim 150$  nm length and aspect ratio,  $\sim 2$ . In the subsequent growth, the aspect ratio of the decahedron increases by 2 - 3.5 times (see growth stages III and IV corresponding to 120 and 150 min thermolysis, respectively). In stage IV, the nanoparticles

become tapered with a large curvature. The intense electric field associated at the tip helps the rapid reduction of Au(I) or Au(III) at the tip [54]. And also the electron liberated in the Ag oxidation moves to the tip of the particles. Au ions present in the reaction reduced at the tip on accepting the electron. It also helps the rapid growth along the  $\langle 110 \rangle$  direction [15]. These led to an extensive longitudinal growth forming eventually forming the  $\mu$ -CPBs (see V - IX in Figure 2.22). The histogram in Figure 2.24 shows the length of the  $\mu$ -CPBs as a function of time. Figure 2.23 represents a schematic of the growth along the  $\langle 110 \rangle$  direction.

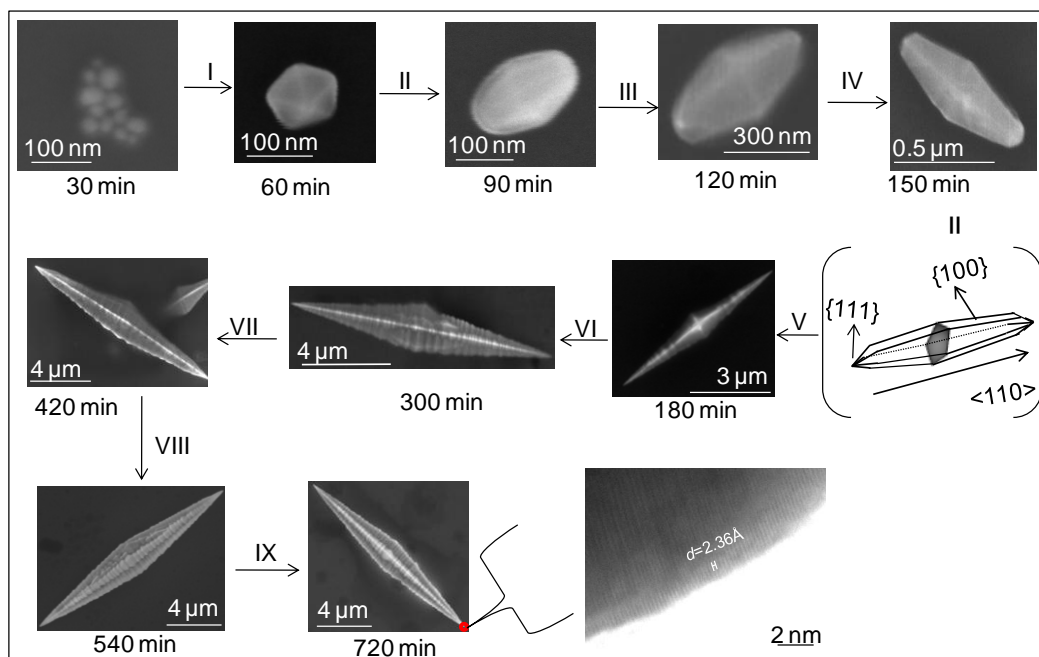


**Figure 2.22** FESEM images collected at different growth times to understand the growth and intermediate stages involved in the formation of the  $\mu$ -CPBs.

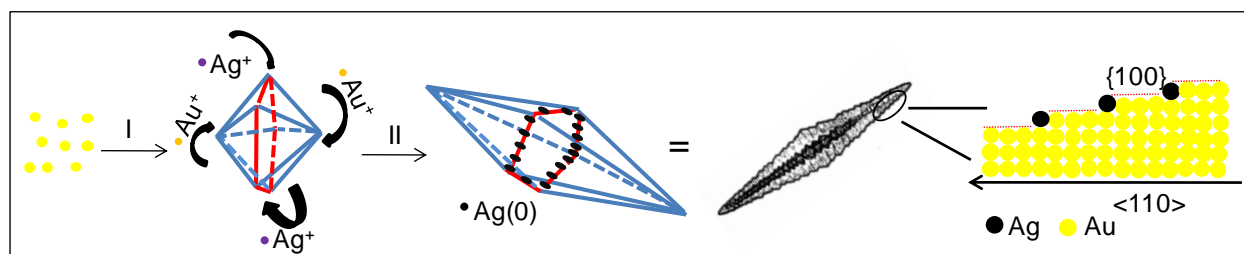


**Figure 2.23** Schematic illustrating the growth mechanism of the  $\mu$ -CPBs along the  $\langle 110 \rangle$ , Ag(+) deposition on Au{100} facets assigned by red color region and Au(I) deposition on Au{111} facets. Cartoon showing the stepped {100} facets stabilized with Ag.

These two growth mechanisms contribute simultaneously to produce longer pentagonal bipyramids with corrugated surface. Ultra-slow rate of the precursor decomposition at 135 °C is also one of the reasons to observe the star shaped structures along the  $\mu$ -CPBs, whereas at higher temperature the sharp branches of the stars are not seen. The ten {111} facets at the tip remain almost unaffected from the seed decahedron to  $\mu$ -CPBs but they are relatively less extended as the  $\mu$ -CPBs grows (HRTEM of the stage IX).

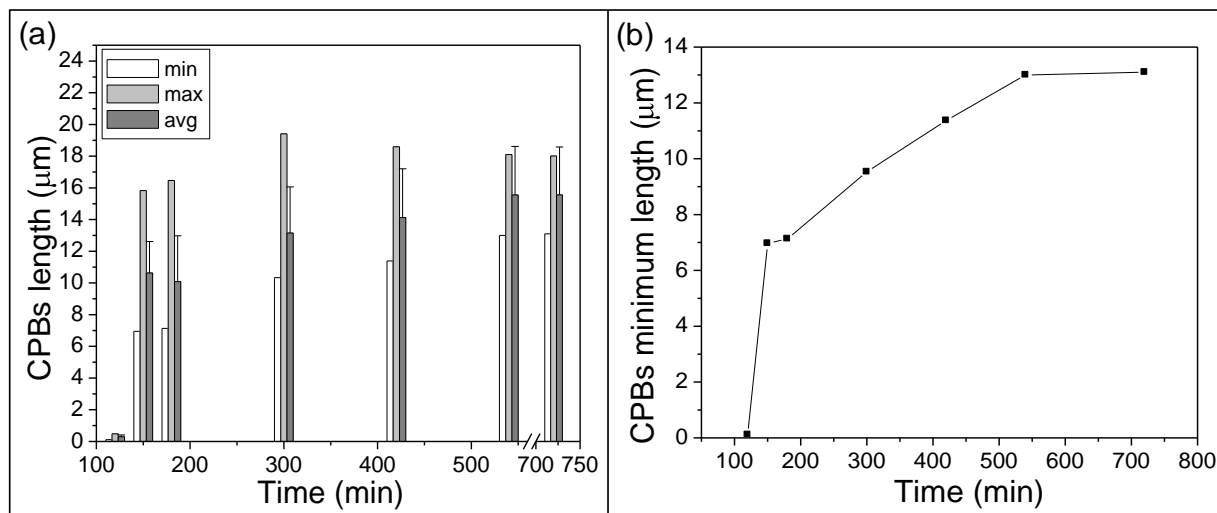


**Figure 2.24** (a) Histogram representing  $\mu$ -CPBs growth as a function of time, and (b)  $\mu$ -CPBs minimum length plotted as a function of time.

The longitudinal growth along the growth axis is rapid than the growth across the particle i.e. the thickness of the particles is lesser than the length of the particle. It is due to the fact that the side facets {100} are adsorbed with Ag. Further, Ag can be oxidized by Au(I), but the kinetics of the Ag displacement by Au(I) is significantly less as Ag-Au dissociation energy is high i.e.,  $47.9 \pm 2.3$  kcal/mole [55], hence the growth on the Au{100} is significantly less. So, Ag can act as a surfactant which inhibits the growth on the Au{100} facets.

While Ag actively participates in the Au  $\mu$ -CPBs growth, it does become part of it. Following the Hume–Rothery rules [56], one would expect an alloy formation, as Ag has similar lattice parameters. Not quite surprisingly, Au-Ag alloy bipyramids (40 - 90 nm) have been reported in the literature starting with  $\text{HAuCl}_4$ ,  $\text{AgNO}_3$  and PVP as a capping agent [22]. In the present method, clearly, Au and Ag though existed in atomic *intimacy*, did not form an alloy. The reason for this unusual behavior is that the Au and Ag precursors separate themselves in different domains when the solvent evaporates from the concoction prior to thermolysis. This became apparent from XRD patterns and

polarizing microscopy images (Figure 2.25) collected from the precursor film, which showed Au-ToABr and Ag-ToABr crystallizing in individual domains.

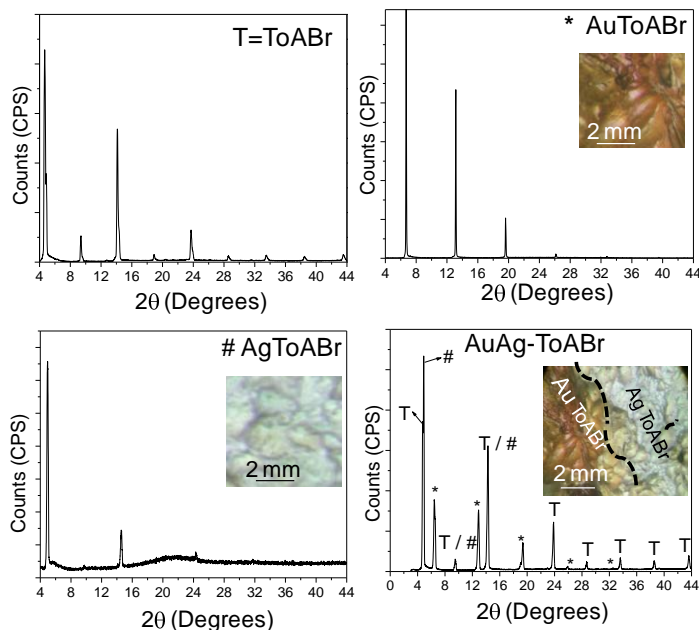


**Figure 2.25** XRD pattern collected from the (a) ToABr, (b) Au ToABr, (c) Ag ToABr, (d) AuAg-ToABr films (T=ToABr, # = Ag-ToABr, \* = Au-ToABr). Inset; polarizing microscopy image of AuAg-ToABr film made by solvent evaporation at the room temperature. Dirty white color region is Ag-ToABr; red color region is Au-ToABr.

### 2.4.c SERS measurements

The surface morphology of the  $\mu$ -CPBs prompts one to use them as SERS substrates. Here, thiophenol (TP) (1mM) and Rhodamine 6G (R6G) (1mM) were used as Raman probe molecules. After chemisorption of these probe molecules, the Raman spectra recorded on individual  $\mu$ -CPBs are shown in Figure 2.26. The SERS spectrum of TP shows significantly intense peaks at 698, 1000, 1023, 1070 and 1576  $\text{cm}^{-1}$ , all assignable to TP. The enhancement factor (G-factor) was calculated from the peak at 1576  $\text{cm}^{-1}$  (corresponding to C=C stretching frequency of phenyl ring).

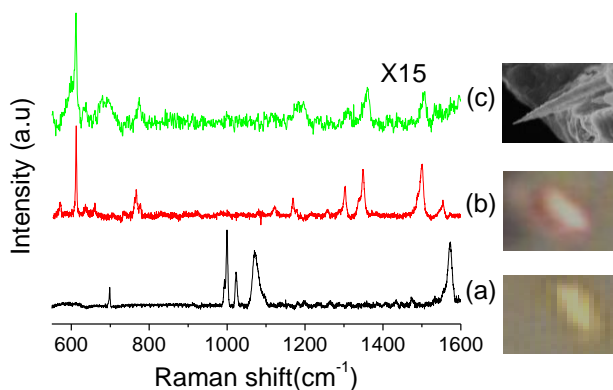


**Figure 2.26** Raman spectra recorded on individual  $\mu$ -CPB particles (optical images shown on the right side) adsorbed with the probe molecules, (a) Thiophenol (TP) and (b) Rhodamine 6G (R6G). The CPBs particles were located on a glass substrate after treatment with 1mM TP, R6G solutions of the probe molecules. In another experiment, a PVP-R6G blend deposited as a film on glass substrate was poked with the tip of a  $\mu$ -CPB and the Raman spectrum (c) was recorded from the tip region. Approximately, 0.5 wt% of PVP polymer was mixed with 1mM R6G/ethanol solution and spin coated onto a cover slip to form a PVP-R6G homogeneous film.

The G-factor was found to be  $2.4 \times 10^6$  for TP. Similarly, Rhodamine 6G (R6G) also gives good SERS spectrum, with a G-factor of  $5.8 \times 10^6$ . The calculations have been done based on a literature procedure [57, 58].

Enhancement factor ( $G$ ) =  $(I_{SERS}/I_{norm}) \times (N_{bulk}/N_{surf})$ , where  $I_{SERS}$  is the measured intensity for the probe molecules,  $I_{norm}$  is the intensity for the bulk sample.

$N_{bulk}$  is the no of particles under illuminated laser beam =  $Ahp/m$ , where A, h,  $\rho$  and m are the area of the laser spot, the penetration depth, the density of probe molecule, and the molecular weight of probe molecule, respectively.

$N_{surf}$  is the no of probe molecules on  $\mu$ -CPBs particles,  $N_{surf} = 4\pi r^2CAN$ , where r, C, A and N are the average radius of nanoparticles, the surface density of thiophenol the area of the focused laser spot, and the surface coverage of particles.

Wang and coworkers reported that due to the lightning rod effect tips of the nanobipyramids or nanorice executed a 6-7 folds higher enhancement than a nanorod having equal volume [13]. Hence, in order to study the efficiency of the tip of  $\mu$ -CPBs *prick and probe* method has performed. This experiment involved the following steps.

*Preparing R6G-PVP blend:* 0.5 wt% of PVP dissolved in 1mM R6G/ethanol solution, PVP-R6G film made on drop coating the solution on a cover slip at 2000 RPM for 8 minutes.

*Fixing  $\mu$ -CPBs to Cu wire:* Cu wire etched with 2.5 M  $\text{FeCl}_3$  until tip of the Cu wire becomes  $\sim 1 \mu\text{m}$ . Cu wire inserted in probe station. Cu wire brought near to the  $\mu$ -CPB as shown in Figure 2.27 (a), 1V bias applied between Si substrate and Cu wire for 100 mS.  $\mu$ -CPB stuck to Cu wire as shown in Figure 2.27b. A  $\mu$ -CPB (Base diameter =  $\sim 1 \mu\text{m}$ ) particle was gently stuck to a Cu wire (diameter =  $\sim 30 \mu\text{m}$ ) and was brought over the PVP-R6G film.

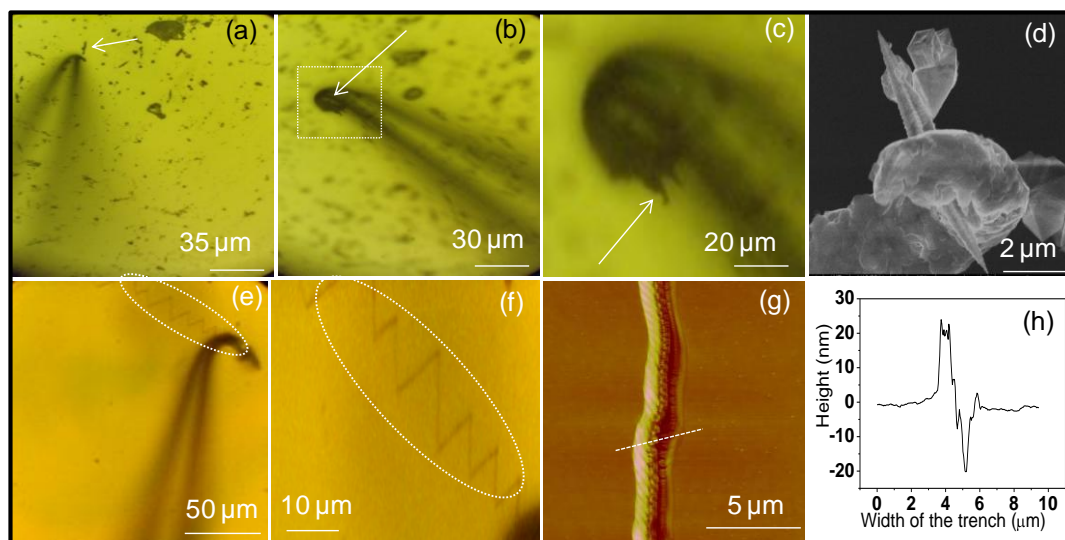


**Figure 2.27** (a-c)  $\mu$ -CPBs manipulation by a Cu wire on a Si substrate. Optical image showing (a) a Cu wire approaching the  $\mu$ -CPB particle (shown by arrow), (b)  $\mu$ -CPB held by the Cu wire and (c) shows a magnified view of the same. (d) FESEM image of a Cu wire carrying the  $\mu$ -CPB, (e) zigzag line (marked by white circle) on a PVP-R6G film made by a  $\mu$ -CPB carried by Cu wire (f) magnified view of zigzag line, (g-h) AFM image of zigzag line and its height profile showing the depth of the line is  $\sim 20 \text{ nm}$  and width of the line is  $\sim 90 \text{ nm}$  which is roughly equal to tip of the  $\mu$ -CPB  $57 \text{ nm}$ .

*Prick the PVP-R6G film and probe through Raman spectroscopy:*  $\mu$ -CPB stuck to Cu wire was brought on to the PVP-R6G film, a zigzag line made by  $\mu$ -CPB stuck to Cu wire on PVP-R6G film as shown in Figure 2.27. The height profile showed that the width of the trench was  $\sim 54 \text{ nm}$  and depth is  $\sim 20 \text{ nm}$ . The probe molecules (R6G) were chemisorbed onto the tip of the  $\mu$ -CPB by leaving the  $\mu$ -CPB particle in contact with the film for 1 hr, Raman performed on the tip of the  $\mu$ -CPB. See Figure 2.28 for the schematic viewing the prick and probe method. Based on the tip radius, the number of adsorbed R6G molecules on the  $\mu$ -CPB tip estimated. All the peaks in the spectrum corresponded to R6G. The above experiment illustrates that even  $\sim 2700$  molecules are sufficient for giving SERS. This prick-and-probe technique for bringing molecules onto the  $\mu$ -CPB SERS substrate ensures the amount of sample required for SERS is minimal, which is very crucial in the case of biomolecules.



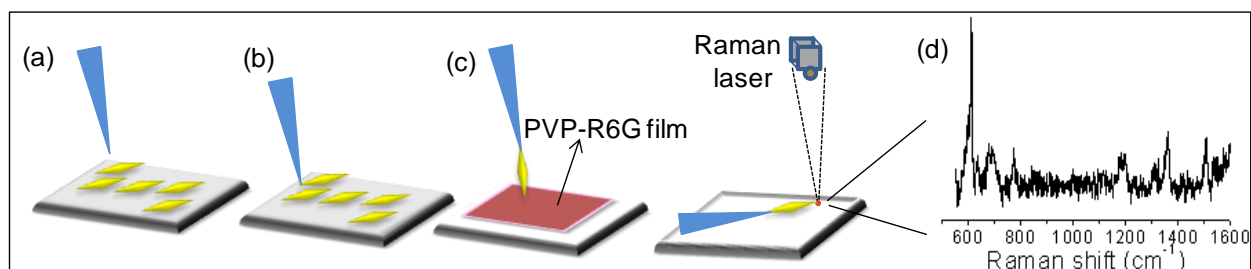


**Figure 2.28** Schematic illustrating the Raman spectrum of PVP-R6G adsorbed at the tip of the  $\mu$ -CPB: (a) Cu wire approaching  $\mu$ -CPB, (b)  $\mu$ -CPB stuck to Cu wire (c) PVP-R6G poked by  $\mu$ -CPB, (d) Raman spectrum obtained from the tip of the  $\mu$ -CPB.

Recently, nanoparticles serving as gene carriers have attracted wide attention [59]. For e.g., Prasad and coworkers have reported sharp-edged carbon bullets as a plant gene carrier [60]. Functionalized three-dimensional tetra pod like ZnO nanostructures have been used for delivering DNA [61]. The  $\mu$ -CPBs presented here could serve as effective gene carrier for the following reasons. Firstly, Au is more bio-compatible than other metals and semiconductor materials. Secondly, ultra sharp pyramidal shaped tips of the  $\mu$ -CPBs would enable easy penetration of the cell membrane with less force, to deliver the desired drug to interior parts of the cell.

## 2.5 Conclusions

$\mu$ -CPBs were synthesized using a simple solid state synthesis. The current method is versatile in that it is a single step solid-state synthesis (unaided by any solvent) and can be carried out on almost any flat substrate that can withstand 130 °C. The growth of  $\mu$ -CPBs can be halted or resumed any time, by simply turning on the hotplate or switching it on. The  $\mu$ -CPBs being long enough can be easily observed using a simple optical microscope. The precursor is highly enriched with metal (~14 wt%) and the thermolysis product is only the reduced metal with hardly any trace of impurities. Although the  $\mu$ -CPBs are entirely made of Au, the presence of  $(\text{AgBr}_2)^-$  ion in the reaction seems to play a key role in tuning the shape of the anisotropic particles. Shape and size of the  $\mu$ -CPBs were tailored by varying the volume ratio of Au(III), Ag(I) and thermolysis temperatures. The growth of the  $\mu$ -CPBs was studied in detail on halting the reaction at various time periods. The  $\mu$ -CPBs serve as excellent SERS substrates. The efficiency of the tip of a  $\mu$ -CPB was studied in a “*prick and probe experiment*”. The tip carrying just 2700 R6G molecules produced a measurable Raman signal.

### References

- [1] Turner M, et al. (2008) Selective oxidation with dioxygen by gold nanoparticle catalysts derived from 55-atom clusters. *Nature* 454(7207):981-983.
- [2] Habouti S, et al. (2011) Self-standing corrugated Ag and Au-nanorods for plasmonic applications. *J. Mater. Chem.*, 21(17):6269-6273.
- [3] Bhuvana T, Kumar GVP, Kulkarni GU, & Narayana C (2007) Carbon Assisted Electroless Gold for Surface Enhanced Raman Scattering Studies. *J. Phys. Chem. C* 111(18):6700-6705.
- [4] Bhuvana T & Kulkarni GU (2009) Femtoliter silver cups as surface enhanced Raman scattering active containers. *Nanotechnology* 20(4):045504.
- [5] Zeng J, et al. (2011) Successive Deposition of Silver on Silver Nanoplates: Lateral versus Vertical Growth. *Angew. Chem. Int . Ed.* 50(1):244-249.
- [6] Kho KW, Shen ZX, Zeng HC, Soo KC, & Olivo M (2005) Deposition Method for Preparing SERS-Active Gold Nanoparticle Substrates. *Anal. Chem.* 77(22):7462-7471.
- [7] Huang X, El-Sayed IH, Qian W, & El-Sayed MA (2006) Cancer Cell Imaging and Photothermal Therapy in the Near-Infrared Region by Using Gold Nanorods. *J. Am. Chem.Soc* 128(6):2115-2120.
- [8] Taton TA, Mirkin CA, & Letsinger RL (2000) Scanometric DNA Array Detection with Nanoparticle Probes. *Science* 289(5485):1757-1760.
- [9] Haes AJ & Van Duyne RP (2002) A Nanoscale Optical Biosensor: Sensitivity and Selectivity of an Approach Based on the Localized Surface Plasmon Resonance Spectroscopy of Triangular Silver Nanoparticles. *J. Am. Chem.Soc* 124(35):10596-10604.
- [10] Li C-Z, Male KB, Hrapovic S, & Luong JHT (2005) Fluorescence properties of gold nanorods and their application for DNA biosensing. *Chem. Commun.* (31):3924-3926.
- [11] Liang H, Yang H, Wang W, Li J, & Xu H (2009) High-Yield Uniform Synthesis and Microstructure-Determination of Rice-Shaped Silver Nanocrystals. *J. Am. Chem.Soc* 131(17):6068-6069.
- [12] Wiley BJ, et al. (2007) Synthesis and Optical Properties of Silver Nanobars and Nanorice. *Nano Letters* 7(4):1032-1036.
- [13] Kou X, et al. (2007) Growth of Gold Bipyramids with Improved Yield and Their Curvature-Directed Oxidation. *Small* 3(12):2103-2113.
- [14] Pelton M, et al. (2009) Damping of acoustic vibrations in gold nanoparticles. *Nat Nano* 4(8):492-495.

- [15] Zheng Y, et al. (2011) Facile Synthesis of Gold Nanorice Enclosed by High-Index Facets and Its Application for CO Oxidation. *Small* 7(16):2307-2312.
- [16] Hasan W, et al. (2009) Tailoring the Structure of Nanopyramids for Optimal Heat Generation. *Nano Letters* 9(4):1555-1558.
- [17] Burgin J, Liu M, & Guyot-Sionnest P (2008) Dielectric Sensing with Deposited Gold Bipyramids. *J. Phys. Chem. C* 112(49):19279-19282.
- [18] Lee S, Mayer KM, & Hafner JH (2009) Improved Localized Surface Plasmon Resonance Immunoassay with Gold Bipyramid Substrates. *Anal. Chem.* 81(11):4450-4455.
- [19] Wu H-L, Chen C-H, & Huang MH (2008) Seed-Mediated Synthesis of Branched Gold Nanocrystals Derived from the Side Growth of Pentagonal Bipyramids and the Formation of Gold Nanostars. *Chem. Mater* 21(1):110-114.
- [20] Jana NR, Gearheart L, Obare SO, & Murphy CJ (2002) Anisotropic Chemical Reactivity of Gold Spheroids and Nanorods. *Langmuir* 18(3):922-927.
- [21] Liu & Guyot-Sionnest P (2005) Mechanism of Silver(I)-Assisted Growth of Gold Nanorods and Bipyramids. *J. Phys. Chem. B* 109(47):22192-22200.
- [22] Zhang X, et al. (2007) Synthesis and Growth Mechanism of Pentagonal Bipyramid-Shaped Gold-Rich Au/Ag Alloy Nanoparticles. *Langmuir* 23(11):6372-6376.
- [23] Zhang S, et al. (2007) Nanonecklaces assembled from gold rods, spheres, and bipyramids. *Chem. Commun.* (18):1816-1818.
- [24] Liang H, Yang H, Wang W, Li J, & Xu H (2009) High-Yield Uniform Synthesis and Microstructure-Determination of Rice-Shaped Silver Nanocrystals. *Journal of the American Chemical Society* 131(17):6068-6069.
- [25] Chen HM, Liu R-S, & Tsai DP (2009) A Versatile Route to the Controlled Synthesis of Gold Nanostructures. *Cryst. Growth Des.* 9(5):2079-2087.
- [26] Mayer KM, Hao F, Lee S, Nordlander P, & Hafner JH (2010) A single molecule immunoassay by localized surface plasmon resonance. *Nanotechnology* 21(25):255503.
- [27] Senapati D, Singh AK, & Ray PC (2010) Real time monitoring of the shape evolution of branched gold nanostructure. *Chemical Physics Letters* 487(1-3):88-91.
- [28] Wang H, Brandl DW, Le F, Nordlander P, & Halas NJ (2006) Nanorice: A Hybrid Plasmonic Nanostructure. *Nano Letters* 6(4):827-832.
- [29] Shen H-x, Yao J-l, & Gu R-a (2009) Fabrication and characteristics of spindle Fe<sub>2</sub>O<sub>3</sub>@Au core/shell particles. *Transactions of Nonferrous Metals Society of China* 19(3):652-656.

- [30] Tran TT & Lu X (2011) Synergistic Effect of Ag and Pd Ions on Shape-Selective Growth of Polyhedral Au Nanocrystals with High-Index Facets. *J. Phys. Chem. C* 115(9):3638-3645.
- [31] Carbo-Argibay E, Rodriguez-Gonzalez B, Pastoriza-Santos I, Perez-Juste J, & Liz-Marzan LM (2010) Growth of pentatwinned gold nanorods into truncated decahedra. *Nanoscale* 2(11):2377-2383.
- [32] Chen H, et al. (2009) Shape-Dependent Refractive Index Sensitivities of Gold Nanocrystals with the Same Plasmon Resonance Wavelength. *J. Phys. Chem. C* 113(41):17691-17697.
- [33] Stockman MI (2011) Erratum: Nanofocusing of Optical Energy in Tapered Plasmonic Waveguides [*Phys. Rev. Lett.* 93, 137404 (2004)]. *Phys. Rev. Lett.* 106(1):019901.
- [34] Hasan W, Lee J, Henzie J, & Odom TW (2007) Selective Functionalization and Spectral Identification of Gold Nanopyramids. *J. Phys. Chem. C* 111(46):17176-17179.
- [35] Nagpal P, Lindquist NC, Oh S-H, & Norris DJ (2009) Ultrasmooth Patterned Metals for Plasmonics and Metamaterials. *Science* 325(5940):594-597.
- [36] Vedantam S, et al. (2009) A Plasmonic Dimple Lens for Nanoscale Focusing of Light. *Nano Lett.* 9(10):3447-3452.
- [37] Offerhaus HL, et al. (2005) Creating Focused Plasmons by Noncollinear Phasematching on Functional Gratings. *Nano Lett.* 5(11):2144-2148.
- [38] Lindquist NC, Nagpal P, Lesuffleur A, Norris DJ, & Oh S-H (2010) Three-Dimensional Plasmonic Nanofocusing. *Nano Lett.* 10(4):1369-1373.
- [39] He W, et al. (2009) Formation of AgPt Alloy Nanoislands via Chemical Etching with Tunable Optical and Catalytic Properties. *Langmuir* 26(6):4443-4448.
- [40] Radha B, Arif M, Datta R, Kundu T, & Kulkarni G (2010) Movable Au microplates as fluorescence enhancing substrates for live cells. *Nano Research* 3(10):738-747.
- [41] Radha B & Kulkarni GU (2010) A Real Time Microscopy Study of the Growth of Giant Au Microplates. *Cryst. Growth Des.* 11(1):320-327.
- [42] Kuisma-Kursula P (2000) Accuracy, precision and detection limits of SEM–WDS, SEM–EDS and PIXE in the multi-elemental analysis of medieval glass. *X-Ray Spectrometry* 29(1):111-118.
- [43] Jiang P, Xie S-s, Yao J-n, Pang S-j, & Gao H-j (2001) The stability of self-organized 1-nonanethiol-capped gold nanoparticle monolayer. *Journal of Physics D: Applied Physics* 34(15):2255.
- [44] Wang P, et al. (2009) Ag/AgBr/WO<sub>3</sub>·H<sub>2</sub>O: Visible-Light Photocatalyst for Bacteria Destruction. *Inorg. Chem.* 48(22):10697-10702.

- [45] Xia Y, Xiong Y, Lim B, & Skrabalak SE (2009) Cover Picture: Shape-Controlled Synthesis of Metal Nanocrystals: Simple Chemistry Meets Complex Physics? (*Angew. Chem. Int. Ed.* 1/2009). *Angew. Chem. Int. Ed.* 48(1):1-1.
- [46] Johnson CJ, Dujardin E, Davis SA, Murphy CJ, & Mann S (2002) Growth and form of gold nanorods prepared by seed-mediated, surfactant-directed synthesis. *J. Mater. Chem.*, 12(6):1765-1770.
- [47] Kou X, et al. (2006) Growth of Gold Nanorods and Bipyramids Using CTEAB Surfactant. *J. Phys. Chem. B* 110(33):16377-16383.
- [48] Elechiguerra JL, Reyes-Gasga J, & Yacaman MJ (2006) The role of twinning in shape evolution of anisotropic noble metal nanostructures. *J. Mater. Chem.*, 16(40):3906-3919.
- [49] Tsuji M, et al. (2008) Toward to branched platinum nanoparticles by polyol reduction: A role of poly(vinylpyrrolidone) molecules. *Colloids and Surfaces A: Physicochem. Eng. Aspects* 317(1-3):23-31.
- [50] Kan C, et al. (2010) Gold Microplates with Well-Defined Shapes. *Small* 6(16):1768-1775.
- [51] Tsuji M, et al. (2009) Stepwise Growth of Decahedral and Icosahedral Silver Nanocrystals in DMF. *Cryst. Growth Des.* 10(1):296-301.
- [52] Sławiński GW, Ivanova OS, & Zamborini FP (2011) Twin Plane Decoration of Silver Nanorods with Palladium by Galvanic Exchange at a Controlled Rate. *Langmuir* 27(21):13293-13301.
- [53] Jiang Q, et al. (2011) Synthesis and high electrocatalytic performance of hexagram shaped gold particles having an open surface structure with kinks. *Nano Research* 4(6):612-622.
- [54] Pérez-Juste J, Liz-Marzán LM, Carnie S, Chan DYC, & Mulvaney P (2004) Electric-Field-Directed Growth of Gold Nanorods in Aqueous Surfactant Solutions. *Adv. Funct. Mater.* 14(6):571-579.
- [55] Pakiari AH & Jamshidi Z (2010) Nature and Strength of M–S Bonds (M = Au, Ag, and Cu) in Binary Alloy Gold Clusters. *J. Phys. Chem. A* 114(34):9212-9221.
- [56] <http://www.msm.cam.ac.uk/phase-trans/2004/titanium/hume.rothery.html>
- [57] Bhuvana T & Kulkarni GU (2008) A SERS-Active Nanocrystalline Pd Substrate and its Nanopatterning Leading to Biochip Fabrication. *Small* 4(5):670-676.
- [58] Mitani Y, et al. (2006) Role of adsorbed water in diffusion of rhodamine 6G on glass surface. *Chemical Physics Letters* 431(1-3):164-168.
- [59] Torney F, Trewyn BG, Lin VSY, & Wang K (2007) Mesoporous silica nanoparticles deliver DNA and chemicals into plants. *Nat Nano* 2(5):295-300.

## Chapter 3

---

- [60] Vijayakumar PS, Abhilash OU, Khan BM, & Prasad BLV (2010) Nanogold-Loaded Sharp-Edged Carbon Bullets as Plant-Gene Carriers. *Adv. Funct. Mater.* 20(15):2416-2423.
- [61] Nie L, et al. (2006) Three-Dimensional Functionalized Tetrapod-like ZnO Nanostructures for Plasmid DNA Delivery. *Small* 2(5):621-625.

## Synthesis of Ag microstructures and their applications in SERS

### Summary

This chapter deals with the synthesis of  $\mu\text{m}$  size Ag cubes, dendrites and polygons. First, AgBr cubes and dendrites have been prepared by the decomposition of the complex,  $(\text{AgCl}_2)\text{-ToABr}$  at different temperatures for 1 hr in air, on a glass substrate. Thermolysis at  $210\text{ }^\circ\text{C}$  resulted in cubes of AgBr with  $\sim 6 - 7\ \mu\text{m}$  sides while at  $250\text{ }^\circ\text{C}$ , AgBr dendrites formed with branches extending over  $\sim 40 - 60\ \mu\text{m}$ . They could be reduced to metallic Ag using aq.  $\text{NaBH}_4$  while nearly maintaining their shapes. Similarly, aq. ammonia solution ( $\text{AgBr}/\text{aq.NH}_3$ ) has been used to prepare AgBr polygons which were reduced to Ag polygons with side lengths of  $\sim 18 - 25\ \mu\text{m}$ . Photoreduction followed by catechol treatment was employed in this case. In general, all Ag structures become roughened and porous. These structures are essentially an assembly of closely packed Ag nanoparticles. When used as SERS substrates, they have shown Raman enhancement of  $\sim 10^6 - 10^7$ .

---

Manuscript based on this work is under preparation

### 3.1 Introduction

Anisotropic metal nanoparticles have been the subject of interest in recent years due to their size and shape dependent physical and chemical properties [1, 2]. Among the coinage metals, Ag has received much attention due to its unique optical properties which can be exploited for a variety of applications [3] such as Surface-enhanced Raman spectroscopy (SERS) [4] and catalysis [5]. Among the different shapes cubes [6], dendrites [7], hexagons [8], rods [9] and wires [10] of Ag are well known. Ag nanocubes of ~100 nm dimension, have been prepared by polyol [11] and modified polyol methods [12]. Dendrites and plate-like structures have been synthesized using various methods [13-22]. Several known synthesis methods for the synthesis nanostructures have drawbacks such as usage of polymers [23-25], high temperatures [26] and long reaction times [27]. The nanostructures of different shapes can have excellent applications in SERS [28-30].

### 3.2 Scope of the investigation

This chapter involves synthesis of micron size Ag particles in the form of cubes, dendrites, polygons using a simple protocol. The additional advantage over reported methods is that this method enables synthesis of micron sized structures having a large number of SERS hot spots. This is in contrast to using complex processes involving lithography and chemical etching methods [31-41].

### 3.3 Experimental details

Silver nitrate ( $\text{AgNO}_3$ ), tetraoctylammonium bromide (ToABr), and toluene were obtained from Sigma Aldrich and used without further purification. The water used throughout this investigation was double distilled and deionized. Si and glass substrates are cleaned with water, IPA, toluene and dried under  $\text{N}_2$  gas.

*(AgCl<sub>2</sub>)-ToABr complex preparation:* Add 1 mL of  $\text{AgNO}_3$  solution (25 mM) to a 1 mL of saturated NaCl solution under stirring, to give rise to a white color colloidal dispersion of AgCl. To this, add a 2 mL of ToABr (50 mM in toluene) while stirring continued. Organic phase contains Ag-ToABr complex, separate and characterizes further. Schematic 3.1 shows an overview of the synthesis procedure of micron size Ag cubes and dendrites.

*AgBr/NH<sub>3</sub> preparation:* To prepare Ag polygons AgBr/NH<sub>3</sub> is used. Initially, AgBr precipitate was obtained by dissolving 60 mg of KBr in 1 mL of aqueous  $\text{AgNO}_3$  (25 mM) under stirring. The



precipitate was washed with water for several times and dried under hot blower. Dry AgBr was dissolved in 1mL of liquor  $\text{NH}_3$ .

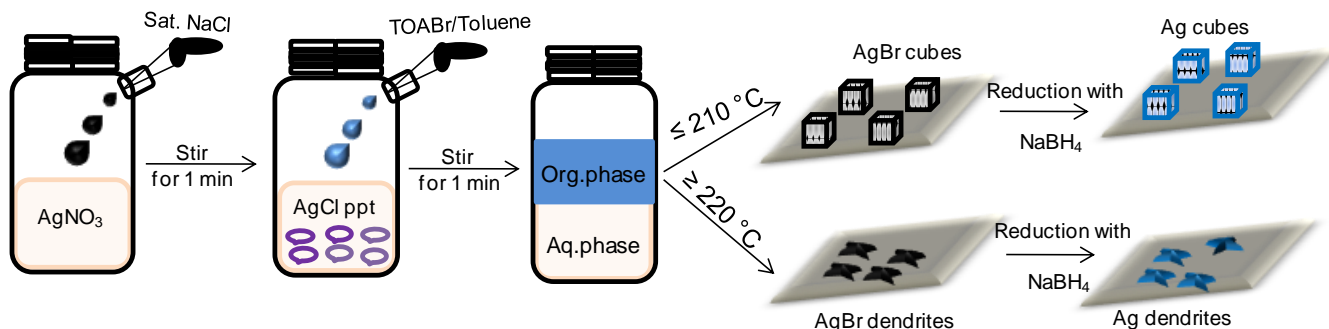


**Figure 3.1** Schematic illustrating the synthetic routes to make cubes and dendrites.

### 3.4 Results and discussion

#### 3.4.a Ag cubes

*AgBr cube preparation:* AgBr cubes were obtained by the decomposition of  $(\text{AgCl}_2)\text{-ToABr}$  at 210 °C on a glass substrate. The substrate was washed with toluene to remove the untreated precursor. A large number of well separated square-like structures were observed (see Figure 3.2a). These have dimensions of 7 - 8  $\mu\text{m}$  (Figure 3.2b) and are of nearly uniform size. The high magnification imaging shows that the square features correspond to cubic structure (see Figure 3.2c). Along with isolated cubes, few pairs oriented in different ways have been found (see inset in Figure 3.2b). The pairs arrange either in edge to edge configuration indicated by 1 or in face to face configuration designated as 2 and 3. All these orientations were observed on a single substrate. The EDS spectrum (see Figure 3.2a) collected from a single cube shows the presence of Ag and Br, and the Si signals is from the glass substrate. The brightness of the edges (Figure 3.2c) is due to charging as the cubes and the substrate are electrically non-conducting. The images are collected in low vacuum mode in order to nullify the charging of the sample.

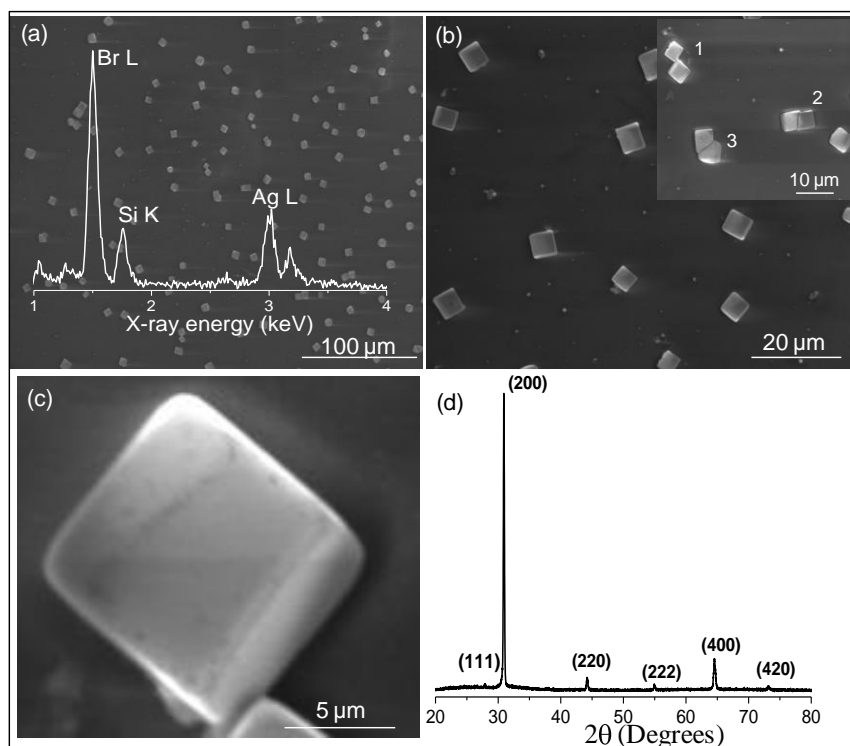


**Figure 3.2** (a-c) FESEM images of AgBr  $\mu$ -cubes on a glass substrate at different magnifications. Inset in Figure 3.2a is the EDS spectrum collected from a single cube, inset in the Figure 3.2b shows the arrangement of two cubes in various configurations. (d) XRD pattern collected from AgBr cubes.

The XRD pattern in Figure 3.2d matches well with polycrystalline cubic AgBr (JCPDS No. 4-0784). As shown in the Table 3.1, it is evident that the (200) plane is the preferred orientation implying that the observed facets correspond to the (100) plane [42].

AgBr plane	JCPDS-06-0438	Cubes	Difference (%)
(200)	100	100	0
(220)	78	6	92.3
(222)	28	4.15	85.1
(400)	16	12.77	20.1
(420)	31	3.71	88.0
(111)	7	0	100
(311)	3	0	100
(331)	16	0	100

**Table 3.1** Comparison of XRD peaks intensities collected from the AgBr cubes with polycrystalline Cubic AgBr (JCPDS 06-0438).

*Reduction to Ag:* AgBr  $\mu$ -cubes have been reduced with 17 mM NaBH<sub>4</sub> aq. solution. After the chemical reduction, the overall morphology of the cubes did not change (see Figure 3.3a). As the reduction with NaBH<sub>4</sub> is vigorous, the structures become rough and porous. As shown in Figure 3.3b, they possess layer like edges. Figure 3.3c is further magnified image; each layer of a cube seems to be composed of Ag nanoparticles with dimensions of  $\sim$  30 - 50 nm forming networks. The trenches shown by arrows may be micro defects, perhaps arising due to the rapid reduction of AgBr. No detectable amount of Br is observed in reduced AgBr cubes (see EDS spectrum in Figure 3.3 inset). The XRD pattern can be assigned to polycrystalline Ag (JCPDS 4-0787) (Figure 3. 3d).

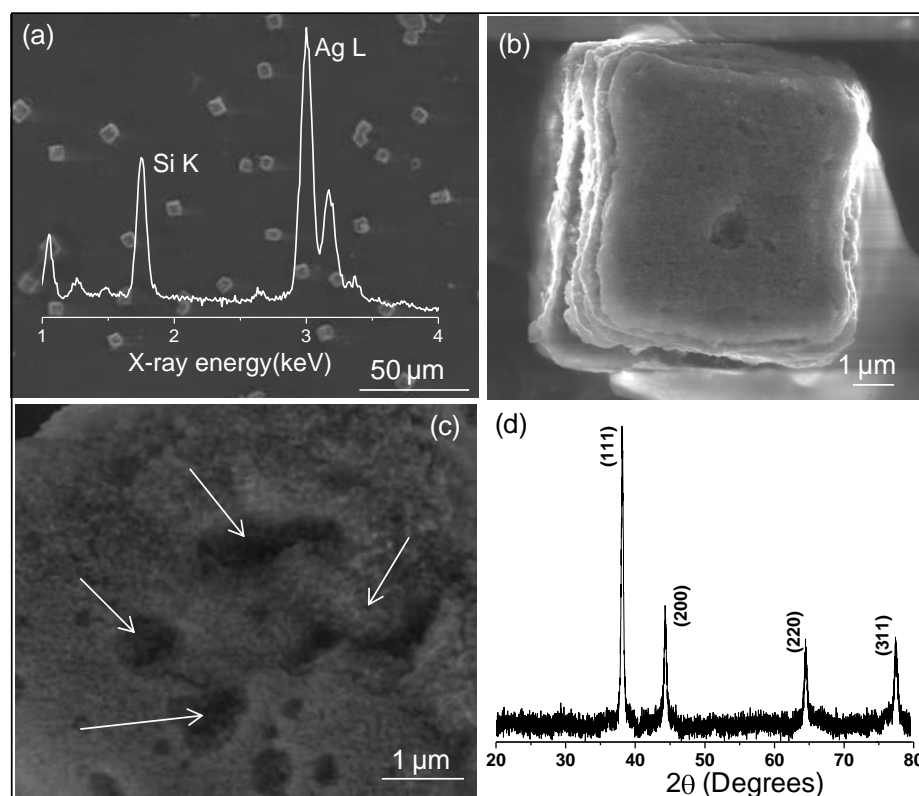


**Figure 3.3** (a-c) FESEM images at different magnifications of Ag cubes obtained by the reduction of the AgBr cubes with NaBH<sub>4</sub>, inset in Figure 3a is the EDS spectrum collected from a single cube, arrows in Figure 3c indicate micro defects arising due to the rapid reduction process and d) XRD pattern collected from the Ag cubes.

### 3.4.b Ag dendrites

*AgBr dendrites preparation and reduction:* Dendrites were obtained by the thermolysis of Ag-ToABr at 250 °C for 1 hr in air (Figure 3.4). Most of them are four branches with each branch extending to 40 - 60  $\mu\text{m}$  (Figure 3.4a). They comprise of Ag and Br as shown in the EDS spectrum in Figure 3.4a. XRD pattern collected from the dendrites shown in Figure 3.4d, matches well with polycrystalline cubic AgBr (JCPDS No. 4-0784). As in the case of cubes, AgBr dendrites were reduced with 17 mM  $\text{NaBH}_4$  aq. solution. As shown in Figure 3.4b, the shape of dendrites retains after reduction. They are highly porous and consist of network structures with nearly  $\sim 70 - 80$  nm as shown in Figure 3.4c. They are of metallic Ag with no detectable bromine as evident in the EDS spectrum (Figure 3.4c). As shown in Figure 3.4d, the XRD pattern matches with polycrystalline Ag (JCPDS 4-0787) (Figure 3.4d).

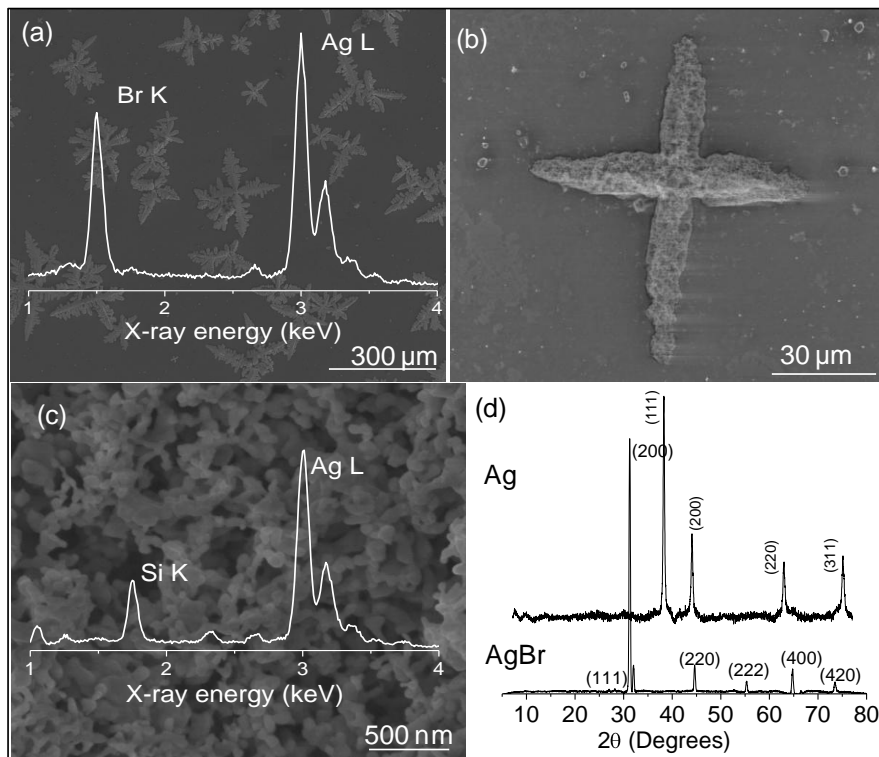


**Figure 3.4** (a) FESEM image of AgBr dendrites, inset is the EDS spectrum collected from a AgBr dendrite. (b - c) Ag dendrites FESEM images at different magnifications, inset in Figure 3c is the EDS spectrum collected from a Ag dendrite and (d) XRD patterns of Ag and AgBr.

TGA shows that the decomposition of the precursor starts at  $\sim 165$  °C (Figure 3.5). Weight loss in TGA occurs in two steps - region I (3%) and regions II (81.46%) correspond respectively to

the solvent evaporation, decomposition, and desorption of ToABr, ToA, and chloride ions, and the AgBr residue (15.54 wt%). Based on TGA, the derived formula is  $(\text{AgCl}_2)\text{ToA}\cdot\text{ToABr}$ , which in a simplified way, is written as Ag-ToABr.

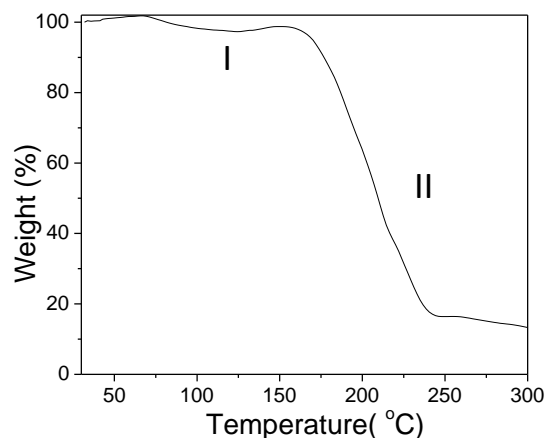


**Figure 3.5** TGA of the precursor showing various stages (I-II) during the decomposition of Ag-ToABr.

Only cubes are observed at lower temperatures of thermolysis, i.e. 190 - 210 °C. Cubes, distorted cubes and smaller dendrites were seen at 220 °C, at higher temperatures (> 220 °C), only dendrites are observed (see Figure 3.6a). The size of the thermolysis product increases as the temperature increases (Figure 3.6b). Figure 3.7 shows optical microscopy images of the AgBr structures obtain at different temperatures of thermolysis.

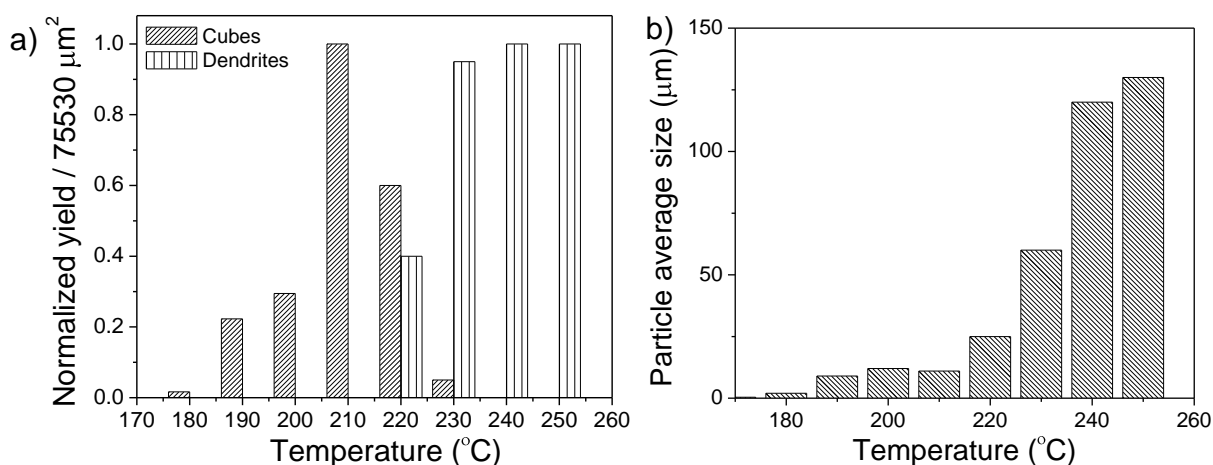


**Figure 3.6** (a) Histogram showing the yield of cubes and dendrites prepared on a glass substrate at different temperatures, (b) plot showing the substrate temperature as a function of set temperature.

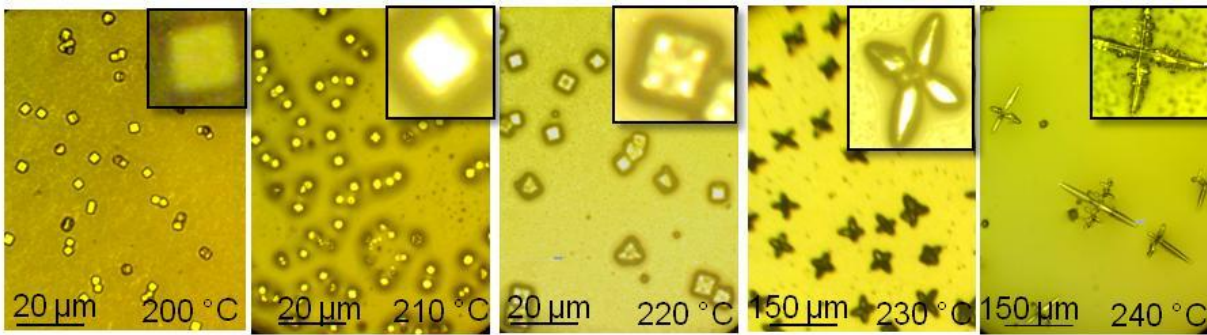


**Figure 3.7** Optical microscopy images of AgBr structures prepared at different temperature (200-240 °C) on a glass substrate and the inset shows the magnified image.

The conversion of cubes to dendrites involves intermediate stages. Initially, the corners of the cubes are sharp, further they become smoothed as the thermolysis temperature increases (see Figure 3.8.1d, b). Sharp corners of the AgBr cubes etched by the precursor to generate cubes with rounded corners (Figure 3.8.2) [43]. The edges of the cubes also etched simultaneously to produce distorted cubes as shown in Figure 3.8.1e. The edges of the cubes acted as growth centers to form branches on the edges of cubes as shown in Figure 3.8.1f. The intermediate stages, Figure 3.8.1d - f are observed from a single substrate. Further growth lead to longer dendrites as shown in Figure 3.8.1g - f. Based on experimental results, the proposed mechanism is shown in Figure 3.8.3.

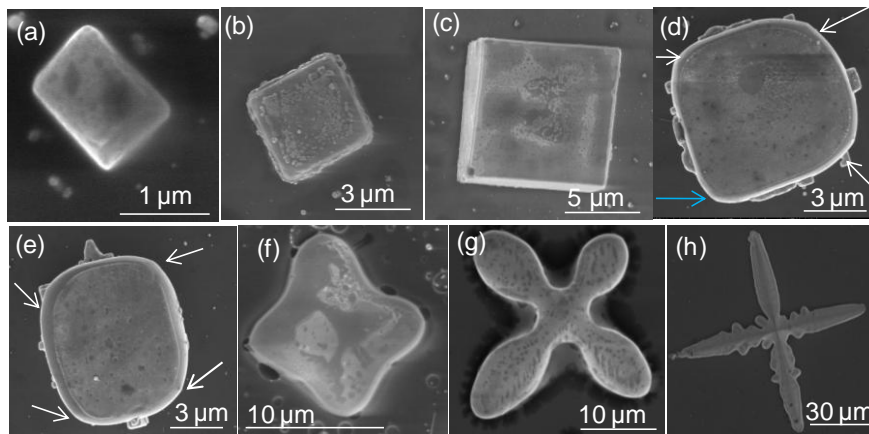


**Figure 3.8.1** FESEM images of AgBr structures have been collected from the samples prepared at different temperatures. (a) 190 °C, (b) 200 °C, (c) 210 °C, (d - e) 220 °C, (g) 230 °C and (h) 240 °C are thermolysis temperatures.

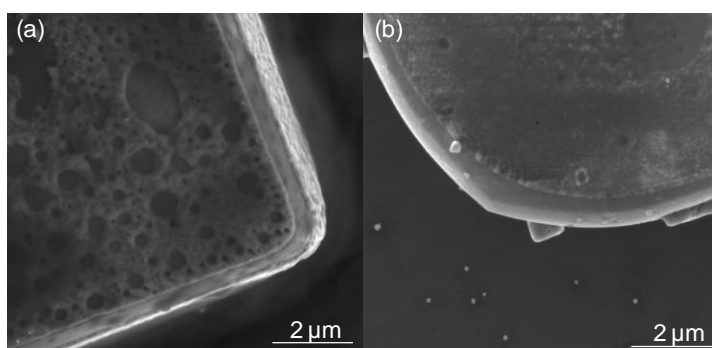


**Figure 3.8.2** (a-b) FESEM image of a cube with sharp edges prepared at 200 - 210 °C and cubes with smooth edges observed at 220 - 230 °C respectively.

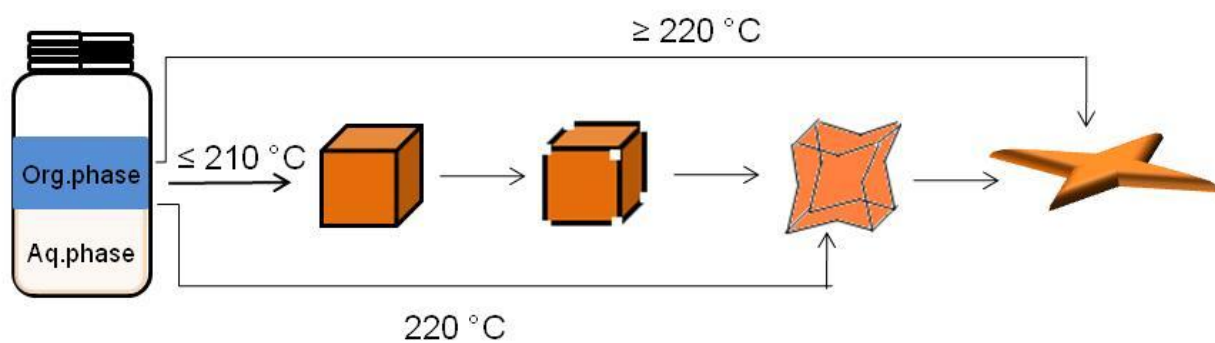


**Figure 3.8.3** Schematic illustrating the growth of formation of the dendrites from the cubes.

Likewise, cubes and dendrites can be prepared on Si substrate with a little variation in the thermolysis temperature.

### 3.4.c AgBr polygons preparation and photoreduction

200  $\mu\text{L}$  of the AgBr/ $\text{NH}_3$  was drop coated on a substrate (Glass or Si). The solvent ( $\text{NH}_3$ ) was left to evaporate at room temperature for  $\sim 20$  min to grow the AgBr polygons. The substrate is washed vigorously with water to remove the excess solvent (see Figure 3.9). It was then dried under  $\text{N}_2$  flow.

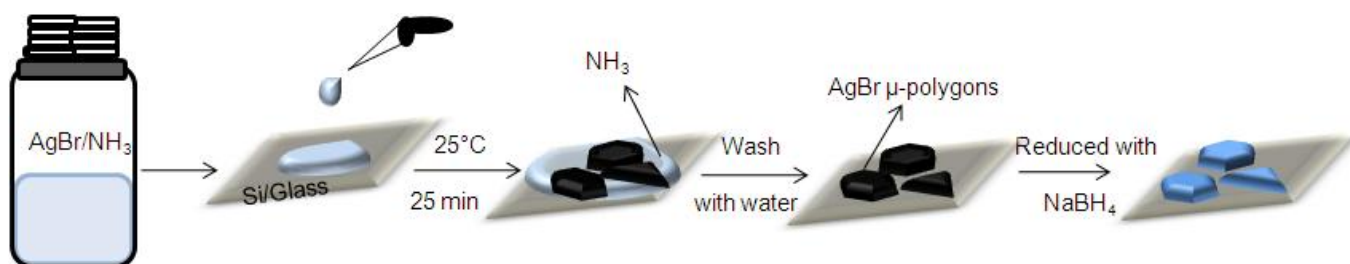


**Figure 3.9** Schematic illustrating the synthetic Ag polygons.

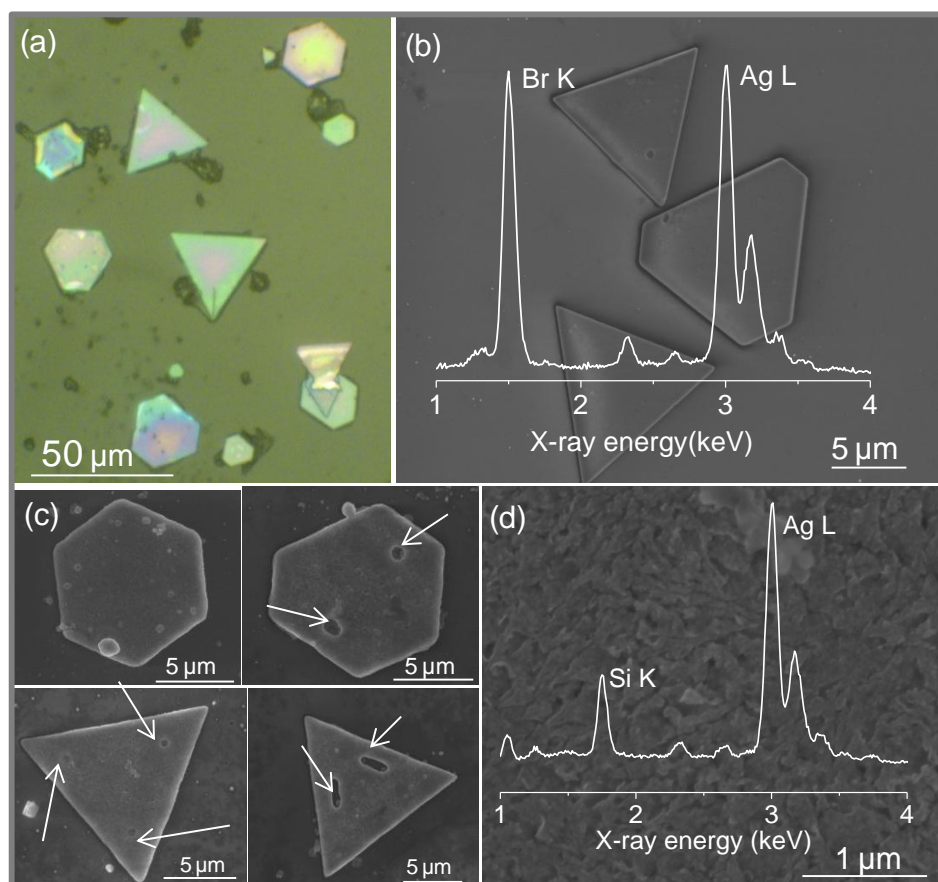


**Figure 3.10** (a) Optical microscopy images of AgBr polygons, (b) FESEM image of AgBr polygons, inset in Figure 3.10b is the EDS from AgBr polygon. (c-d) FESEM images of Ag polygons at different magnifications, inset in Figure 3.10d is the EDS from Ag polygon.

The AgBr polygons are exposed to UV radiation for 30 minutes for initial reduction which could be only partial. Complete reduction of polygons is achieved by alkaline catechol treatment under UV irradiation. Here mild reducing agent catechol used to control the surface roughness and porosity of the polygons. Polygon side length is 18-25  $\mu\text{m}$  as shown in the Figure 3.10 and the thickness is  $\sim 500$  nm. After reduction, the surface roughness increased by a factor of five and causes  $\mu\text{m}$  size trenches shown by arrows in Figure 3.10c. Before reduction, Ag and Br are observed in EDS mapping (see Figure 3.11), while only Ag is observed after reduction (see Figure 3.10d).



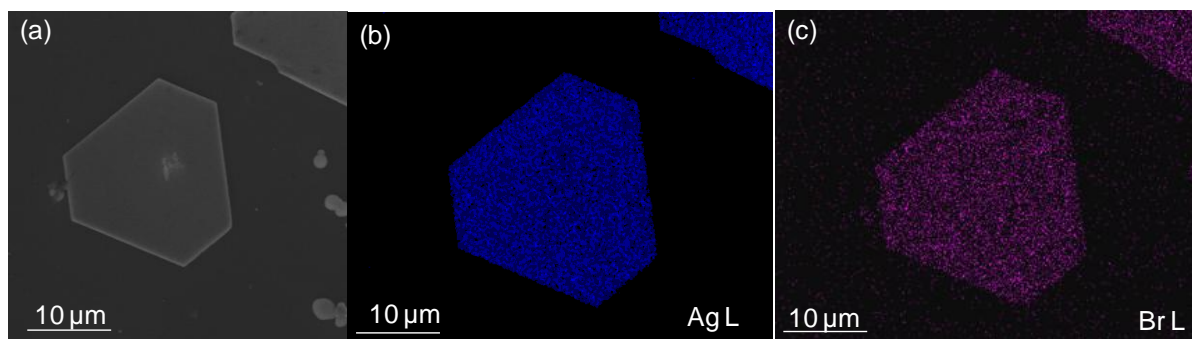


**Figure 3.11** (a) FESEM images of a AgBr polygon, (b-c) EDS mapping obtained for Ag L and Br L energy levels respectively.

XRD pattern collected from the polygons matches with the polycrystalline FCC AgBr (JCPDS 06-0438). Figure 3.12 shows the XRD pattern collected at the various stages involved in the AgBr photoreduction. After 30 min UV irradiation, the major peak of AgBr i.e., (200) plane intensity got diminished by a factor of 4. Amidst AgBr peaks, a new peak appeared at  $\sim 38.1^\circ$  corresponding to the Ag(111) plane. It indicates partial reduction of AgBr. Even after 1 hr irradiation, not much difference observed from the 30 min irradiation. Metallic Ag present on the surface inhibits the complete reduction of the polygon, and it catalyzes further reduction of the polygons with alkaline catechol [44].

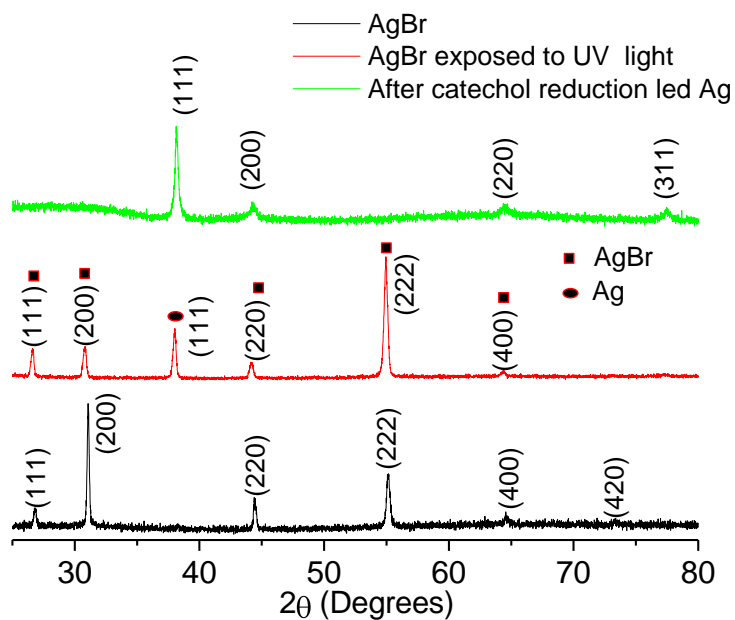


**Figure 3.12** XRD pattern collected at the different stages of the AgBr photoreduction.

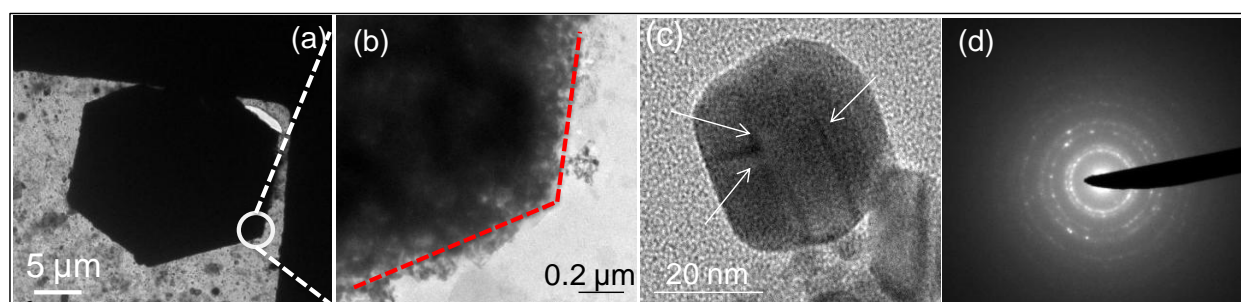


**Figure 3.13** (a-c) TEM images of Ag polygons at different magnifications, (d) ED pattern collected from the one edge of the Ag polygon.

Ag polygons are observed under TEM (Figure 3.13a). They are composed of nanoparticles having 20–40 nm in size as shown in Figure 3.13b. These nanoparticles are separated by less than 10 nm. The nanoparticles shown in Figure III.13c possess defects indicated by the arrows. The circular ED pattern shows the polycrystalline nature of the polygons (see Figure 3.13d).

### 3.4.d SERS measurements

All the synthesized Ag structures were immersed in 1 mM thiophenol/ethanol solution for 6 hours, washed with ethanol and dried at room temperature. Raman spectra were collected from the cubes, dendrites and polygons.

#### *SERS on Ag cubes*

SERS properties of single isolated Ag cube, dimers and trimers of cubes have been measured. For a single cube, Raman spectrum was collected just around the centre. For dimers and trimers, Raman measurement was done at the intersection of the cubes. The characteristic peaks of thiophenol appear at 997, 1021, 1076 and 1574  $\text{cm}^{-1}$ . As shown in Figure III.14a, neat thiophenol has a peak at 1580  $\text{cm}^{-1}$  corresponding to the phenyl stretching mode. This mode is downshifted to 1574  $\text{cm}^{-1}$  when thiophenol adsorbs on the Ag cubes. It is due to the phenyl group interacting with the metal surface [45]. Single cube enhanced the Raman signal by  $\sim 1.1 \times 10^6$ ; in the case of the dimers, the enhancement factor is between  $2.7 \times 10^6$  to  $5.5 \times 10^6$ . Here, the configuration of the cubes plays a role in the enhancement of Raman signal. Face to face configuration has a better enhancement than a single cube. It is due to presence of large number of junctions (see Figure 3.12d) between the adjacent faces of two cubes which act as hot spots.

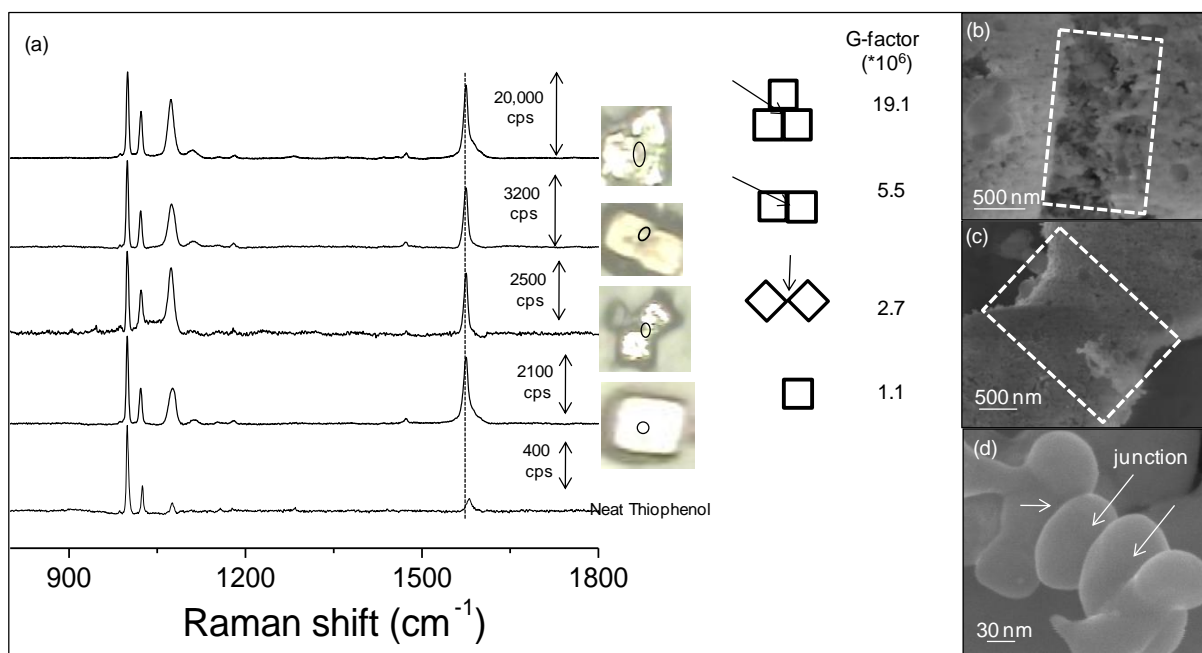


**Figure 3.14** (a) SERS spectra collected from single, dimer and trimer cubes, Raman spectrum collected from the area shown by the black circle. Optical microscopy images of the Ag cubes and cartoons representing the configuration of the cubes and the Raman probed area indicated by an arrow mark. Enhancement factor (g-factor) showed in each case, high resolution FESEM images are collected from the intersection point of the dimer cubes oriented in (b) face to face, (c) edge to edge configuration, (d) junctions (hot spots regions) formed by the assembly of the nanoparticles are shown by the arrows.

As shown in Figure 3.14b the region shown by the rectangular have large number of junctions formed by the Ag particles. Whereas less enhancement is observed at the edge to edge configuration due to the presence of the less number of junctions (see Figure 3.14c) [46]. Most interestingly, Ag trimer has shown nearly 17.3 times of enhancement than that seen for an isolated cube and 3.4 – 7 times enhancement than that from a dimer, respectively. It is due the existence of large number of the junctions [47].

#### *SERS on a dendrite*

Raman spectra are collected from the various parts of the Ag dendrite. As shown in Figure 3.15a, corner and tips of the flower shows higher enhancement. It was due to the presence of large number of hot shops generated at the junction between the nanoparticles indicated by the arrows (see

Figure 3.15b [48, 49]. A lower enhancement was observed at the center, due to the relatively less number of junctions (hot spots) as shown in Figure 3.15b.

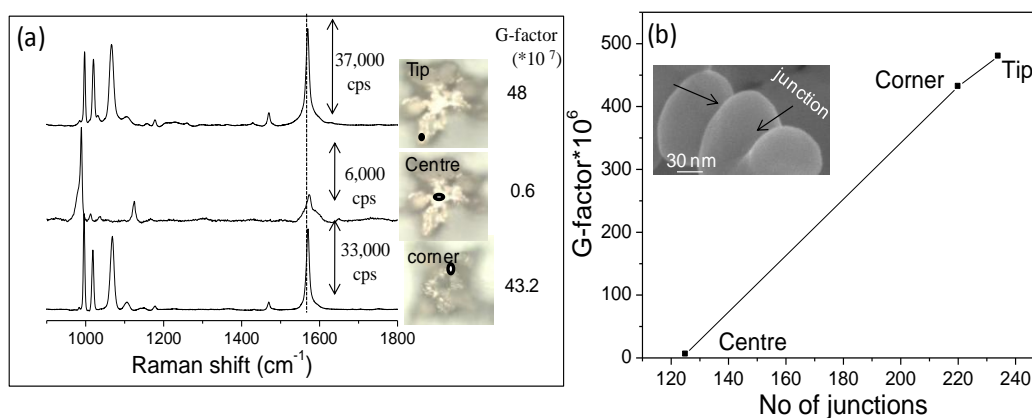


**Figure 3.15** (a) SERS spectra collected from the different regions (shown by black color) of dendrites, (b) plot showing G-factor enhancement as function of no of intersecting points at the different places of a dendrite.

On some cases, the central portion of the dendrites gets removed during the process of the reduction. This might be one of the reasons to observe lesser enhancement. The junction spacing was < 30 nm which is reported in literature as an optimized distance for better enhancement [47]. The roughened surface [50, 51] and highly continuous Ag particles networks were also responsible for showing higher enhancement [52].

### *SERS on a polygon*

As shown in the left hand inset in Figure 3.16, the polygons are composed of nanoparticles which are separated by distances less than 25-30 nm. These clustering of nanoparticles created many hotspots for strong enhancement of Raman signals. The enhancement factor calculated for the 1575 cm<sup>-1</sup> which corresponds to the phenyl ring stretching frequency is  $2.7 \times 10^7$ . Among all these structures Ag dendrites have shown higher enhancement. This is due to the presence of more closely spaced junctions formed by the Ag particles at tips and edges of the dendrites [49].

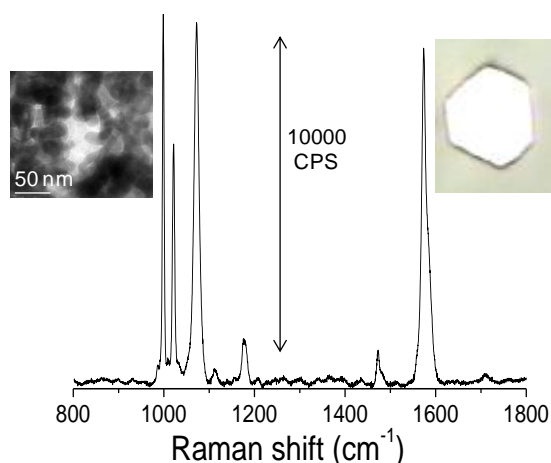


**Figure 3.16** SERS spectrum of thiophenol adsorbed on a Ag polygon, optical microscopy image of a polygon (right hand side) and TEM image taken from the centre portion of the polygon shown in the left hand side.

Along with SERS, Ag plates have been used as a platform for fluorescence studies. Metal nanoparticles are known to show enhancement in the fluorescence of a fluorophore. Metal enhanced fluorescence is due to the coupling between the fluorophore dipole and surface plasmon resonance oscillations of the nearby metal particles decrease the non-radiative rate fluorescence. This phenomenon is said to be MEF [53, 54].

#### 3.4.e Metal enhanced fluorescence

R6G dye was used as a fluorophore to study the MEF on the Ag polygons. 200  $\mu\text{L}$  of 1  $\mu\text{M}$  R6G solution was drop coated on the Ag polygons and AgBr polygons. After complete solvent evaporation, fluorescent measurements were performed. R6G did not get adsorbed on the AgBr surface as shown in Figure 3.17 while it got uniformly adsorbed on the Ag polygon. The enhancement from R6G adsorbed on the Ag polygons is on an average, 10 times more than the R6G adsorbed on the cover slip.

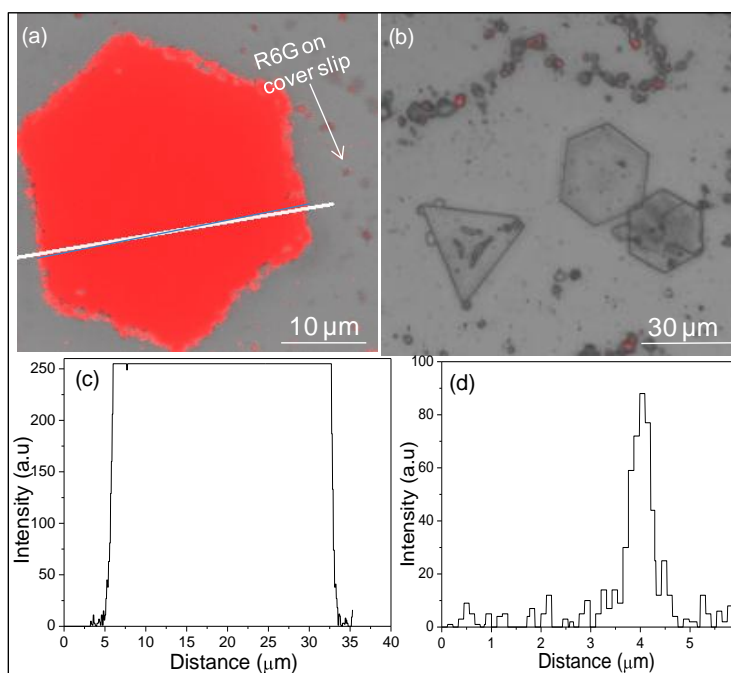


**Figure 3.17** (a-b) Confocal microscopy images of R6G adsorbed on Ag and AgBr polygon respectively, (c-d) intensity profile of R6G adsorbed on a Ag polygons (intensity measured along the line drawn across the polygon) and cover slip.

### 3.5 Conclusions

Micron size cubes and dendrites were prepared with a single precursor by changing the reaction conditions and polygons were prepared by the solvent evaporation. Highly roughened surfaces were obtained by chemical reduction and relatively lesser roughness observed with photoreduction. All μm structures are composed of Ag nanoparticles separated by few tens of nanometers. These gaps are known as hot spot regions and these hot spots enhance the Raman signal. Thus, these are discrete micron sized platforms consisting of hot spots useful as SERS substrates.

### References

- [1] Sau TK & Rogach AL (2010) Nonspherical Noble Metal Nanoparticles: Colloid-Chemical Synthesis and Morphology Control. *Advanced Materials* 22(16):1781-1804.
- [2] Sajanlal PR, Sreeprasad TS, Samal AK, & Pradeep T (2011) Anisotropic nanomaterials: structure, growth, assembly, and functions.
- [3] Rycenga M, et al. (2011) Controlling the Synthesis and Assembly of Silver Nanostructures for Plasmonic Applications. *Chem. Rev* 111(6):3669-3712.
- [4] Anderson DJ & Moskovits M (2006) A SERS-Active System Based on Silver Nanoparticles Tethered to a Deposited Silver Film. *The Journal of Physical Chemistry B* 110(28):13722-13727.
- [5] Cong H, Becker CF, Elliott SJ, Grinstaff MW, & Porco JA (2010) Silver Nanoparticle-Catalyzed Diels–Alder Cycloadditions of 2'-Hydroxychalcones. *Journal of the American Chemical Society* 132(21):7514-7518.
- [6] Skrabalak SE, Au L, Li X, & Xia Y (2007) Facile synthesis of Ag nanocubes and Au nanocages. *Nat. Protocols* 2(9):2182-2190.
- [7] Fang J, et al. (2007) Dendritic Silver Nanostructure Growth and Evolution in Replacement Reaction. *Crystal Growth & Design* 7(5):864-867.
- [8] An J, et al. (2007) Photoinduced Shape Evolution: From Triangular to Hexagonal Silver Nanoplates. *The Journal of Physical Chemistry C* 111(49):18055-18059.
- [9] Zhang J, Langille MR, & Mirkin CA (2011) Synthesis of Silver Nanorods by Low Energy Excitation of Spherical Plasmonic Seeds. *Nano Letters* 11(6):2495-2498.
- [10] Li X, Wang L, & Yan G (2011) Review: Recent research progress on preparation of silver nanowires by soft solution method and their applications. *Crystal Research and Technology* 46(5):427-438.
- [11] Sun Y & Xia Y (2002) Shape-Controlled Synthesis of Gold and Silver Nanoparticles. *Science* 298(5601):2176-2179.
- [12] Im SH, Lee YT, Wiley B, & Xia Y (2005) Large-Scale Synthesis of Silver Nanocubes: The Role of HCl in Promoting Cube Perfection and Monodispersity. *Angewandte Chemie International Edition* 44(14):2154-2157.
- [13] Chen S & Carroll DL (2002) Synthesis and Characterization of Truncated Triangular Silver Nanoplates. *Nano Letters* 2(9):1003-1007.

- [14] Zhang J, Langille MR, & Mirkin CA (2010) Photomediated Synthesis of Silver Triangular Bipyramids and Prisms: The Effect of pH and BSPP. *Journal of the American Chemical Society* 132(35):12502-12510.
- [15] Chaudhari VR, Haram SK, Kulshreshtha SK, Bellare JR, & Hassan PA (2007) Micelle assisted morphological evolution of silver nanoparticles. *Colloids and Surfaces A: Physicochemical and Engineering Aspects* 301(1-3):475-480.
- [16] Charles DE, et al. (2009) Versatile Solution Phase Triangular Silver Nanoplates for Highly Sensitive Plasmon Resonance Sensing. *ACS Nano* 4(1):55-64.
- [17] He X, Zhao X, Chen Y, & Feng J (2008) The evidence for synthesis of truncated triangular silver nanoplates in the presence of CTAB. *Materials Characterization* 59(4):380-384.
- [18] Roh J, Yi J, & Kim Y (2010) Rapid, Reversible Preparation of Size-Controllable Silver Nanoplates by Chemical Redox. *Langmuir* 26(14):11621-11623.
- [19] Iyer KS, Bond CS, Saunders M, & Raston CL (2008) Confinement of Silver Triangles in Silver Nanoplates Templated by Duplex DNA. *Crystal Growth & Design* 8(5):1451-1453.
- [20] Gu C & Zhang T-Y (2008) Electrochemical Synthesis of Silver Polyhedrons and Dendritic Films with Superhydrophobic Surfaces. *Langmuir* 24(20):12010-12016.
- [21] Lai Y, Pan W, Zhang D, & Zhan J (2011) Silver nanoplates prepared by modified galvanic displacement for surface-enhanced Raman spectroscopy. *Nanoscale* 3(5):2134-2137.
- [22] Kim J-Y, Kim SJ, & Jang D-J (2009) Laser-induced shape transformation and electrophoretic analysis of triangular silver nanoplates. *Journal of Separation Science* 32(23-24):4161-4166.
- [23] Ali Umar A, Oyama M, Mat Salleh M, & Yeop Majlis B (2010) Formation of Highly Thin, Electron-Transparent Gold Nanoplates from Nanoseeds in Ternary Mixtures of Cetyltrimethylammonium Bromide, Poly(vinyl pyrrolidone), and Poly(ethylene glycol). *Crystal Growth & Design* 10(8):3694-3698.
- [24] Jiang L-P, et al. (2004) Ultrasonic-Assisted Synthesis of Monodisperse Single-Crystalline Silver Nanoplates and Gold Nanorings. *Inorganic Chemistry* 43(19):5877-5883.
- [25] Xiong Y, et al. (2006) Poly(vinyl pyrrolidone): A Dual Functional Reductant and Stabilizer for the Facile Synthesis of Noble Metal Nanoplates in Aqueous Solutions. *Langmuir* 22(20):8563-8570.
- [26] Du J, Han B, Liu Z, Liu Y, & Kang DJ (2007) Control Synthesis of Silver Nanosheets, Chainlike Sheets, and Microwires via a Simple Solvent–Thermal Method. *Crystal Growth & Design* 7(5):900-904.



- 
- [27] Courty A, Henry AI, Goubet N, & Pileni MP (2007) Large triangular single crystals formed by mild annealing of self-organized silver nanocrystals. *Nat Mater* 6(11):900-907.
- [28] Cobley C, Skrabalak S, Campbell D, & Xia Y (2009) Shape-Controlled Synthesis of Silver Nanoparticles for Plasmonic and Sensing Applications. *Plasmonics* 4(2):171-179.
- [29] , Carraro C, & Maboudian R (2010) Silver Dendrites from Galvanic Displacement on Commercial Aluminum Foil As an Effective SERS Substrate. *Journal of the American Chemical Society* 132(5):1476-1477.
- [30] Chen H, Simon F, & Eychmuller A (2010) Large-Scale Synthesis of Micrometer-Sized Silver Nanosheets. *The Journal of Physical Chemistry C* 114(10):4495-4501.
- [31] Abalde-Cela S, et al. (2010) Surface-enhanced Raman scattering biomedical applications of plasmonic colloidal particles. *Journal of The Royal Society Interface* 7(Suppl 4):S435-S450.
- [32] Bhuvana T & Kulkarni GU (2009) Femtoliter silver cups as surface enhanced Raman scattering active containers. *Nanotechnology* 20(4):045504.
- [33] García-Vidal FJ & Pendry JB (1996) Collective Theory for Surface Enhanced Raman Scattering. *Physical Review Letters* 77(6):1163-1166.
- [34] Xu H, Aizpurua J, Käll M, & Apell P (2000) Electromagnetic contributions to single-molecule sensitivity in surface-enhanced Raman scattering. *Physical Review E* 62(3):4318-4324.
- [35] Chen G, et al. (2009) High-Purity Separation of Gold Nanoparticle Dimers and Trimers. *Journal of the American Chemical Society* 131(12):4218-4219.
- [36] Diebold ED, Peng P, & Mazur E (2009) Isolating Surface-Enhanced Raman Scattering Hot Spots Using Multiphoton Lithography. *Journal of the American Chemical Society* 131(45):16356-16357.
- [37] Fromm DP, Sundaramurthy A, Schuck PJ, Kino G, & Moerner WE (2004) Gap-Dependent Optical Coupling of Single “Bowtie” Nanoantennas Resonant in the Visible. *Nano Letters* 4(5):957-961.
- [38] Kumar GVP, et al. (2007) Hot Spots in Ag Core–Au Shell Nanoparticles Potent for Surface-Enhanced Raman Scattering Studies of Biomolecules. *The Journal of Physical Chemistry C* 111(11):4388-4392.
- [39] Kiristopuryan A, et al. (2009) High-throughput fabrication of nanoantennae over large areas for biosensing and nanospectroscopy. *Applied Physics Letters* 95(23):231903.
- [40] Yim T-J, Wang Y, & Zhang X (2008) Synthesis of a gold nanoparticle dimer plasmonic resonator through two-phase-mediated functionalization. *Nanotechnology* 19(43):435605.

- [41] Bhuvana T & Kulkarni GU (2008) A SERS-Active Nanocrystalline Pd Substrate and its Nanopatterning Leading to Biochip Fabrication. *Small* 4(5):670-676.
- [42] Chen D, Qiao X, Qiu X, Chen J, & Jiang R (2010) Convenient, rapid synthesis of silver nanocubes and nanowires via a microwave-assisted polyol method. *Nanotechnology* 21(2):025607.
- [43] Chen J, et al. (2006) Facile Synthesis of Gold–Silver Nanocages with Controllable Pores on the Surface. *Journal of the American Chemical Society* 128(46):14776-14777.
- [44] <http://www.imaging.org/IST/store/epub.cfm?abstrid=8385>
- [45] Gao P & Weaver MJ (1985) Surface-enhanced Raman spectroscopy as a probe of adsorbate-surface bonding: benzene and monosubstituted benzenes adsorbed at gold electrodes. *The Journal of Physical Chemistry* 89(23):5040-5046.
- [46] Camargo PHC, Au L, Rycenga M, Li W, & Xia Y (2010) Measuring the SERS enhancement factors of dimers with different structures constructed from silver nanocubes. *Chemical Physics Letters* 484(4-6):304-308.
- [47] Qin L, et al. (2006) Designing, fabricating, and imaging Raman hot spots. *Proceedings of the National Academy of Sciences* 103(36):13300-13303.
- [48] Zhou J, Xu S, Xu W, Zhao B, & Ozaki Y (2009) In situ nucleation and growth of silver nanoparticles in membrane materials: a controllable roughened SERS substrate with high reproducibility. *Journal of Raman Spectroscopy* 40(1):31-37.
- [49] Liang H, Li Z, Wang W, Wu Y, & Xu H (2009) Highly Surface-roughened “Flower-like” Silver Nanoparticles for Extremely Sensitive Substrates of Surface-enhanced Raman Scattering. *Advanced Materials* 21(45):4614-4618.
- [50] Ward DR, et al. (2007) Electromigrated Nanoscale Gaps for Surface-Enhanced Raman Spectroscopy. *Nano Letters* 7(5):1396-1400.
- [51] Zheng J, Li X, Gu R, & Lu T (2002) Comparison of the Surface Properties of the Assembled Silver Nanoparticle Electrode and Roughened Silver Electrode. *The Journal of Physical Chemistry B* 106(5):1019-1023.
- [52] Feng F, et al. (2009) SERS detection of low-concentration adenine by a patterned silver structure immersion plated on a silicon nanoporous pillar array. *Nanotechnology* 20(29):295501.
- [53] [http://cfs.umbi.umd.edu/cfs/reprints/rde/cchts\\_6\\_109.pdf](http://cfs.umbi.umd.edu/cfs/reprints/rde/cchts_6_109.pdf)

- [54] Aslan K, Lakowicz JR, & Geddes CD (2005) Metal-enhanced fluorescence using anisotropic silver nanostructures: critical progress to date. *Analytical and Bioanalytical Chemistry* 382(4):926-933.